Detection of B-Mode Polarization at Degree Angular Scales by BICEP2

signature of the gravitational wave in the cosmic inflation

BICEP2

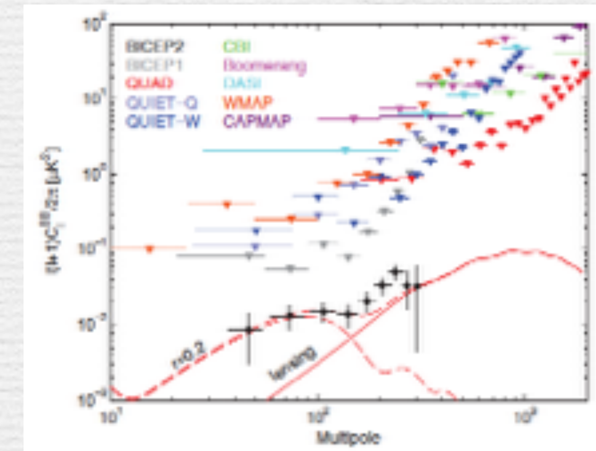

cosmic

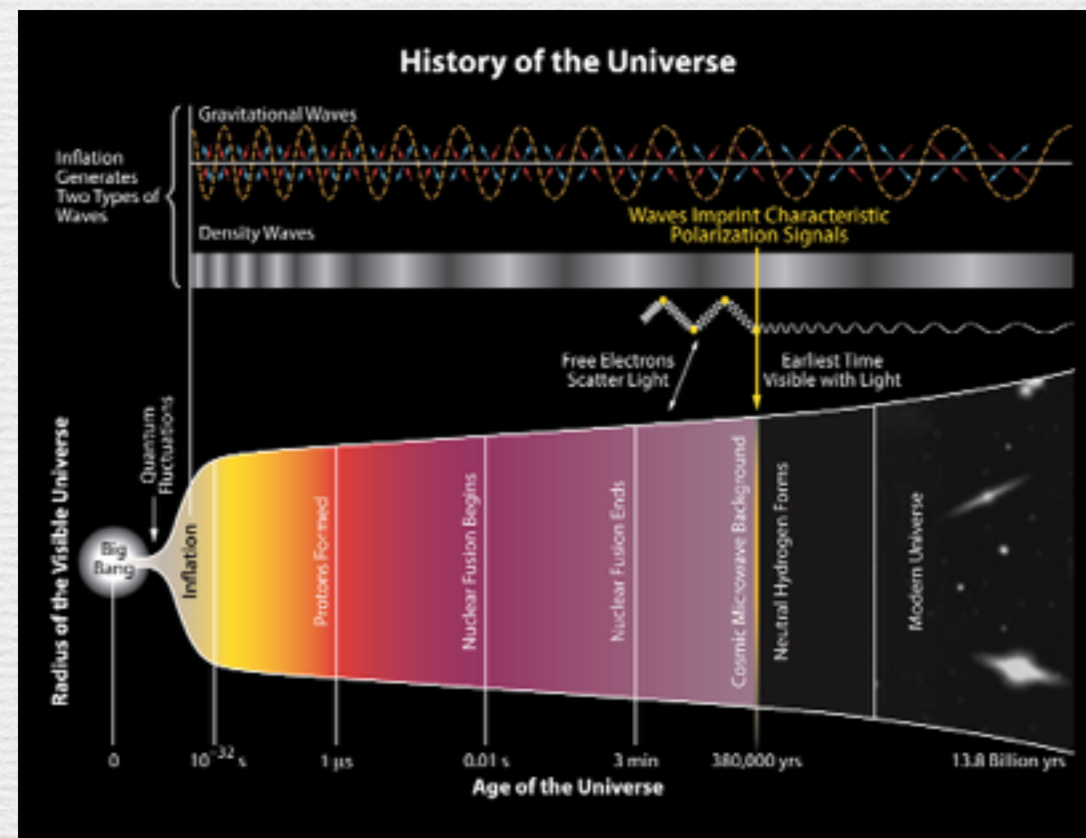

B-mode polarization in CMB

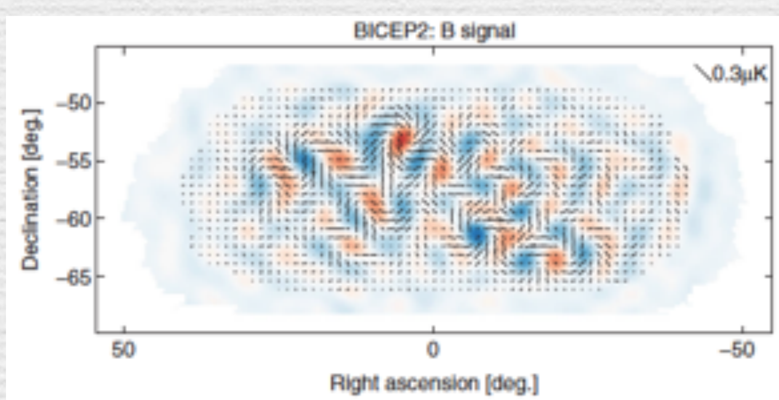

RCNP核理1aグループ勉強会 2014.11.19 by A. Tamii

Introduction

Phys. Rev. Lett.

The Physical Review Letters journal has published an exceptionally long article on the report of measurement of the polarization of cosmic microwave background (

First announcement in preprint in March 2014.

PRL publication in June 2014.

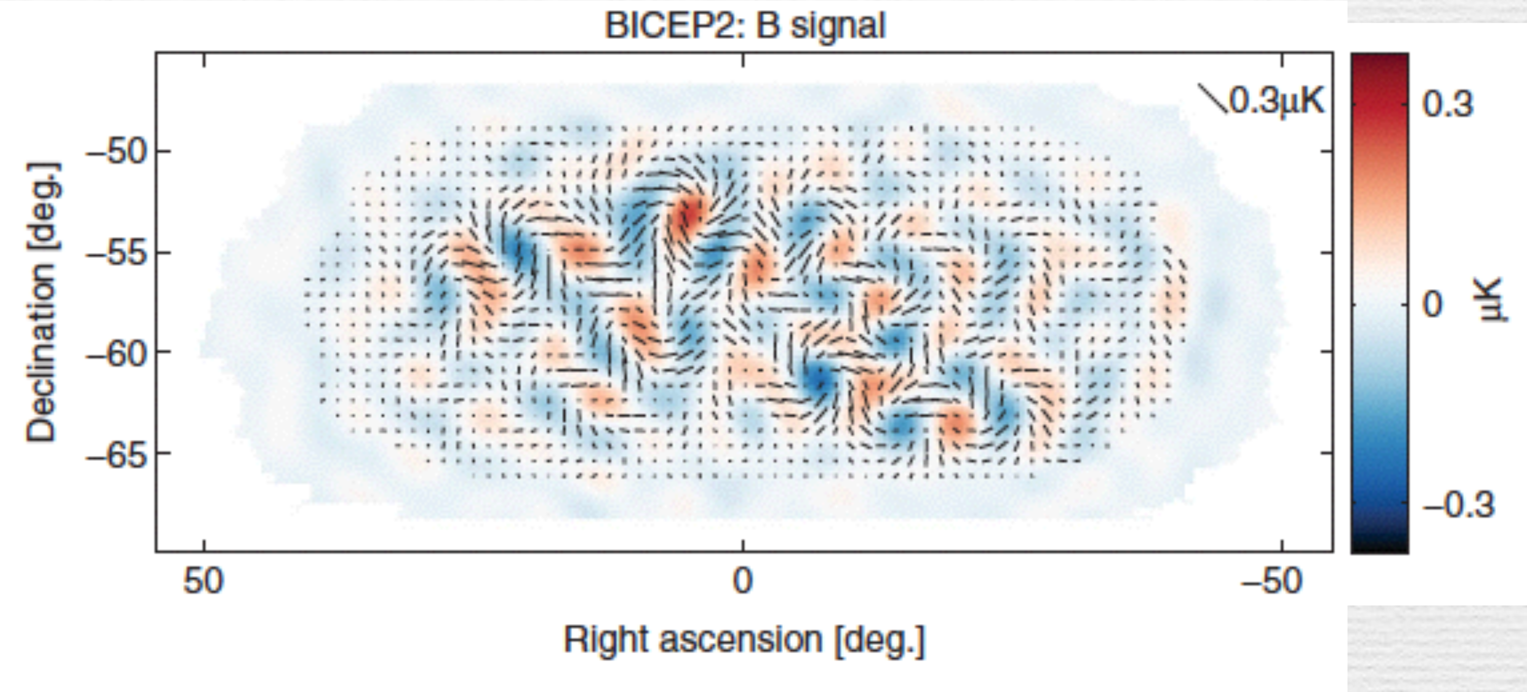

The BICEP2 collaboration has claimed that they found an evidence of the cosmic inflation by detecting a B-mode polarization of the CMB, which could be produced by the strong gravitational wave in the quantum fluctuation during the inflation process.

The result has brought much discussions including physics that can be deduced from it, alternative explanations, and criticism.

Cosmic Microwave Background (CMB)

Evidence of the Big-Bang
(at 13.8 billion years ago)
predicted by G. Gamow

1964 Arno Penzias and Robert W. Wilson
1978 Nobel Prise

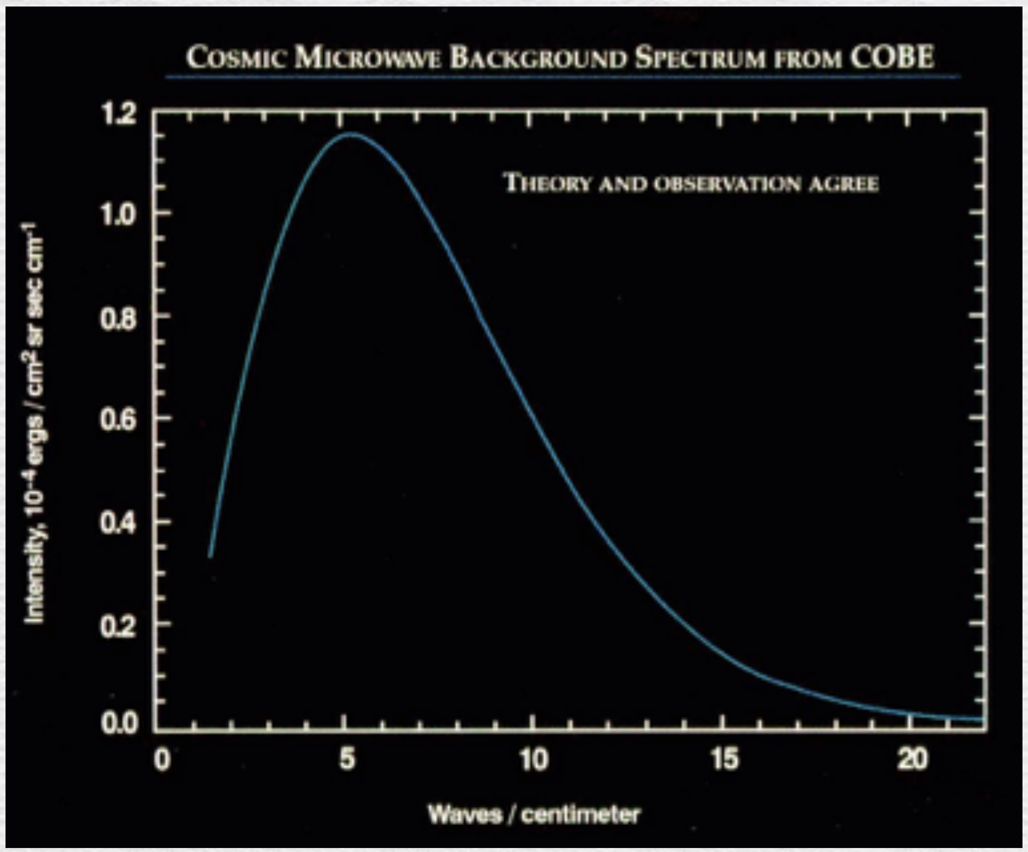

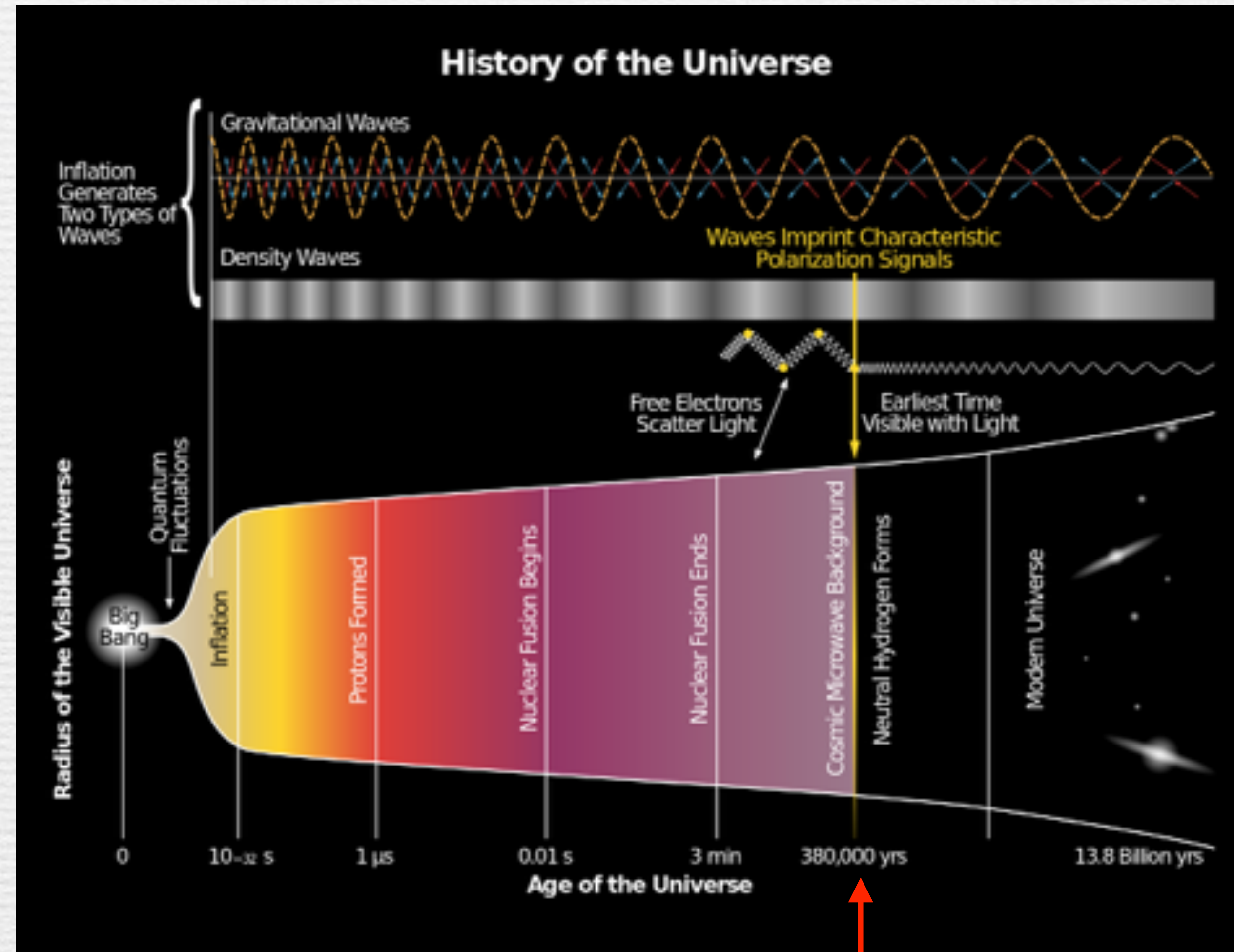

Black Body Radiation

$$K_{\nu}(T) = \frac{h\nu^3}{c^2} \frac{1}{\exp(h\nu / kT) - 1}$$

T

Creation of the present CMB
at the recombination epoch
p+e

Cosmic Inflation

The cosmic inflation was proposed independently
by K. Sato (1981), A. H. Guth (1981), A.D. Linde (1982), et al.,
to solve the misters of flatness, smoothness, monopole problem, etc.

From the age of 10
exponentially with the factor of 10

Note that the difference of the present size of the universe
(10^{26}

The inflation is considered to be driven by the release of the latent heat due to the spontaneous symmetry breaking and the phase transition of the vacuum.

Katsuhiko Sato

Alan H. Guth

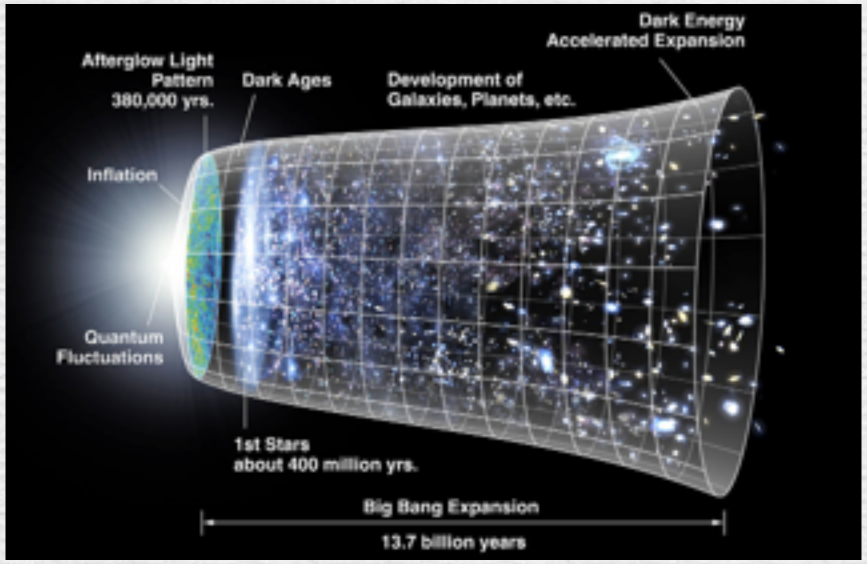

Inflation Model

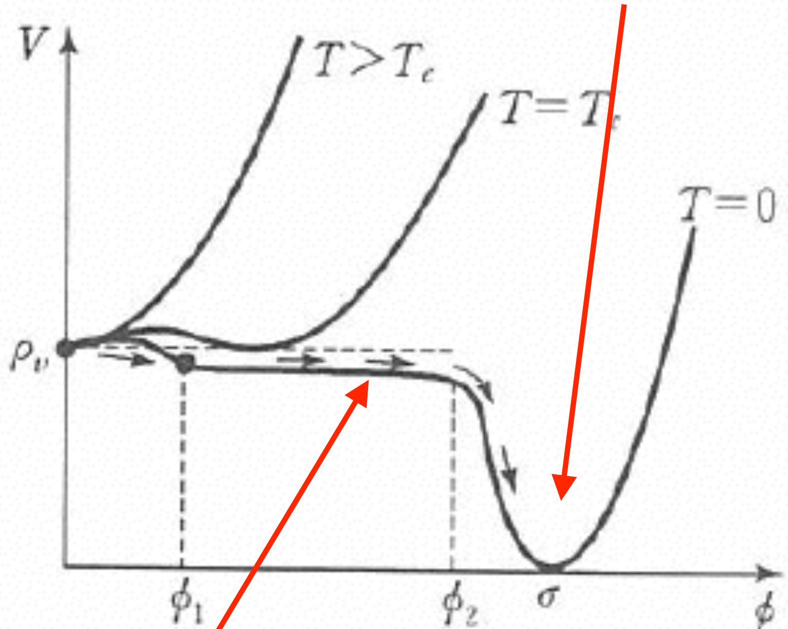

図 8.2　インフレーションモデル
(slow rollover model)

$\phi=0\sim\phi_1$ では1次相転移で偽真空の中に真の真空の泡が発生する．$\phi=\phi_1\sim\phi_2$ ではゆっくりと滑り落ちる（インフレーション期）．$\phi>\phi_2$ では急速に σ に到達した後，σ のまわりの減衰振動（ヒッグスの生成と崩壊）で再加熱し最終的には σ に落ちつく．

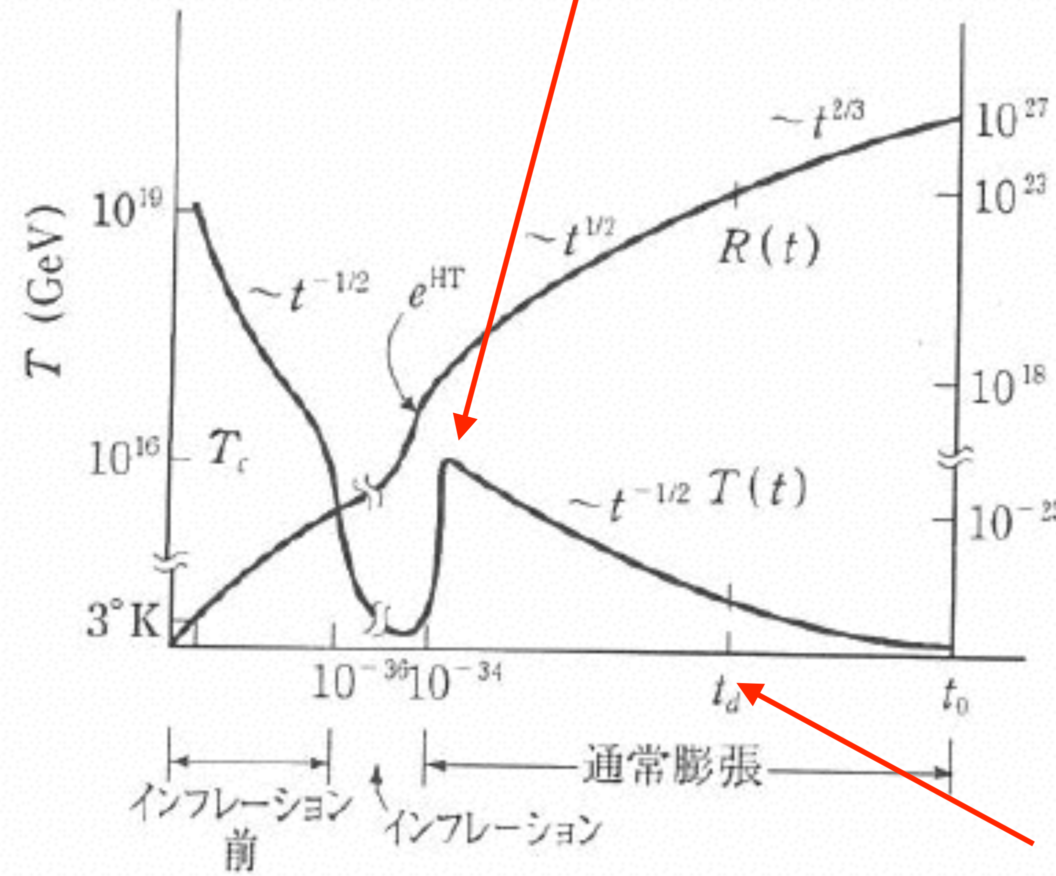

図 8.3　インフレーションシナリオでの温度 T と宇宙サイズ R の時間変化

$t\lesssim10^{-36}$ 秒はインフレーション前期で $R\sim T^{-1}\sim t^{1/2}$，$10^{-36}\lesssim t\lesssim10^{-34}$ 秒はインフレーション期で，$R\sim T^{-1}\sim e^{Ht}$．この期間に宇宙は，$e^{100}\sim10^{43}$ 倍となる．インフレーション終了後再加熱があり，再び $R\sim t^{1/2}$ となり，$t=t_{eq}\doteqdot t_{dc}\sim10^{10}$ 秒で物質優勢の世界となり，$R\sim T^{-1}\sim t^{2/3}$ で進行する（スケールは任意）．

Robertson Walker metric

$$ds^2 = dt^2 - R(t)^2\left[\frac{dr^2}{1-kr^2} + r^2\left(d\theta^2 + \sin^2\theta d\phi^2\right)\right]$$

$$d\Omega^2 = d\theta^2 + \sin^2\theta d\phi^2$$

k
k
k
k

Friedmann equations

$$H^2(t) = \left(\frac{\dot{R}}{R}\right)^2 = \frac{8\pi G}{3}\rho - \frac{k}{R^2} + \frac{\Lambda}{3}$$

R(
H(t)
G: gravitational constant
ρ(t): energy density of the universe
Λ

Energy Conservation

$$\frac{d}{dt}\left(\rho R^3\right) + P\frac{dR^3}{dt} = 0$$

ρ_c: critical density = corresponds to the density at k=0 (flat universe).

$\Omega = \rho/\rho$

At present time

H

ρ_c

h = 0.6~0.8: incompleteness of the observation

1 pc = 3.26 light year

M

Recombination (

At
The universe became transparent.

The photons decoupled at this epoch are the origin of the present cosmic microwave background (CMB).

The present temperature of the CMB is

The age of the universe at the time of recombination is

In the radiation dominant epoch (before ~recombination)

R H ρ

In the matter dominant epoch (after

R H ρ

The present age of the universe

t_0

Time factor = 3×10

Radius factor ~1000
= degree scale

Problem of the horizon

The distance of the present horizon is

$$d_{H0}(t_0) = ct_0 \sim 10^{26}\,\text{m}$$

= the size of the observable universe.

The horizon at the time of recombination

$$d_H(t_{dc}) = ct_{dc}$$

The present horizon at the time of recombination is

$$d_{H0}(t_{dc}) = \frac{R(t_{dc})}{R(t_0)} d_{H0}(t_0)$$

Thus

$$\frac{d_{H0}(t_{dc})}{d_H(t_{dc})} = \frac{R(t_{dc})}{R(t_0)} \frac{d_{H0}(t_0)}{d_H(t_{dc})} = \frac{R(t_{dc})}{R(t_0)} \frac{t_0}{t_{dc}} = \left(\frac{t_{dc}}{t_0}\right)^{2/3} \frac{t_0}{t_{dc}} \sim 100$$

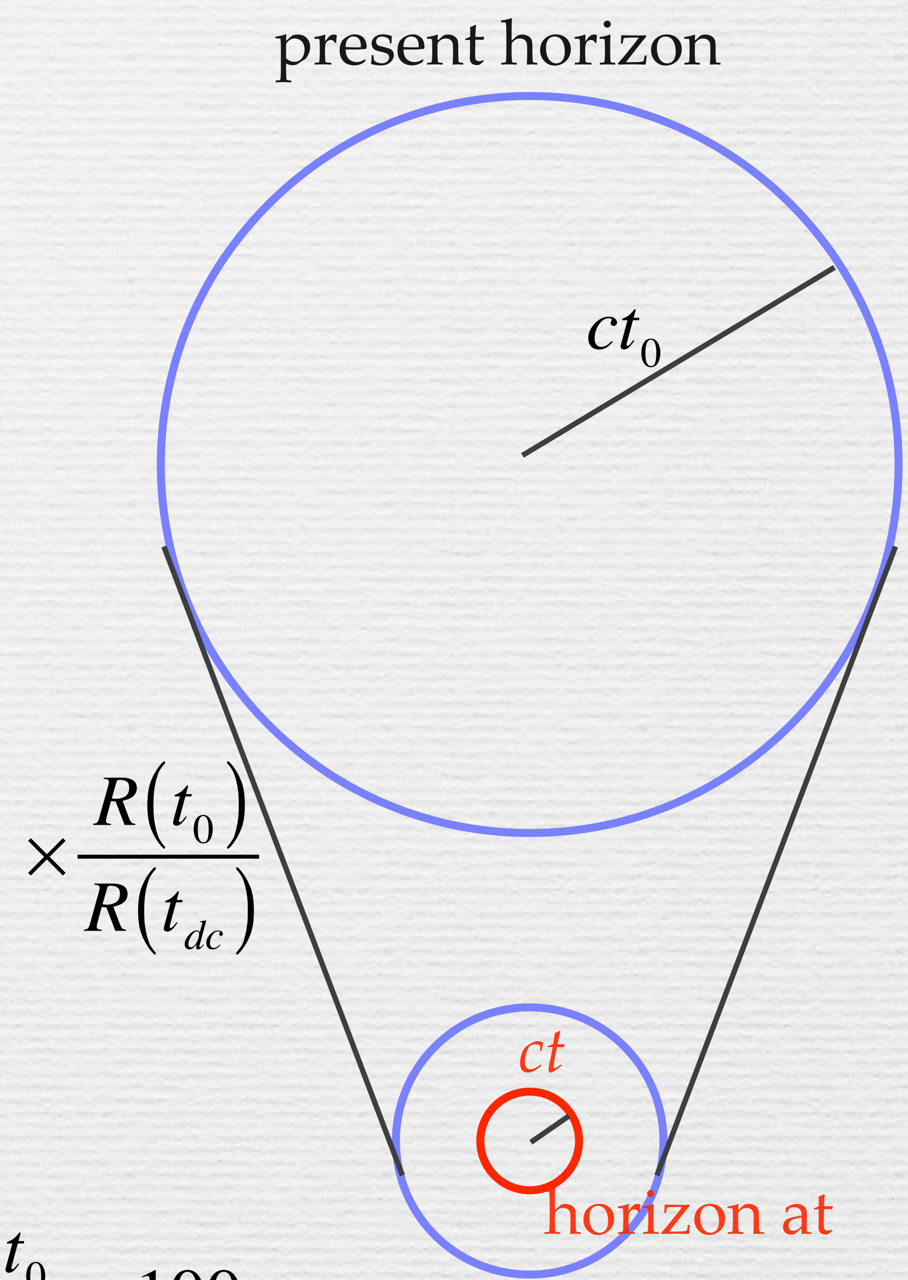

The present horizon at the time of recombination is much larger than the horizon at that time.

→ The uniformity (

The cosmic inflation leads $\frac{d_{H0}(t_{dc})}{d_H(t_{dc})} = 10^{-17}$

Problem of the flatness

The present density of the universe is

$$\Omega_0 = \frac{\rho}{\rho_c} = 0.1 \sim 0.3$$ close to unity

The density at the time of GUT (10

$$\Omega - 1 = \frac{\rho - \rho_c}{\rho_c} = \frac{k}{R^2(t)} H^{-2}(t) = \frac{k}{\dot{R}^2}$$

$$\frac{\Omega(t_{GUT}) - 1}{\Omega_0 - 1} = \left(\frac{t_{GUT}}{t_{dc}}\right)\left(\frac{t_{dc}}{t_0}\right)^{2/3}$$

$$\Omega(t_{GUT}) - 1 = \begin{cases} -10^{-51} & \text{for } \Omega_0 = 0.1 \\ +10^{-51} & \text{for } \Omega_0 = 2.0 \end{cases}$$

Thus the density must have extraordinary close to unity at the time of GUT

The cosmic inflation leads naturally

R

Large-Scale Structure of the Universe

Could be produced by quantum fluctuation expanded by the inflation.

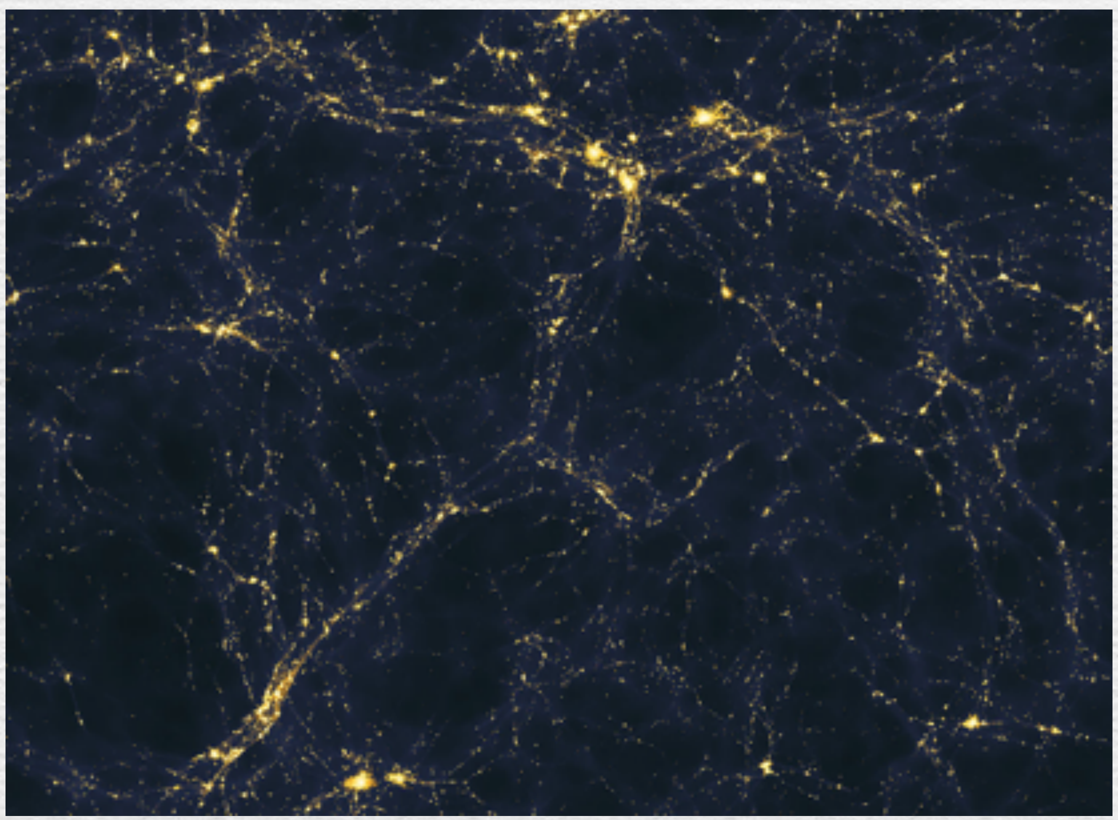

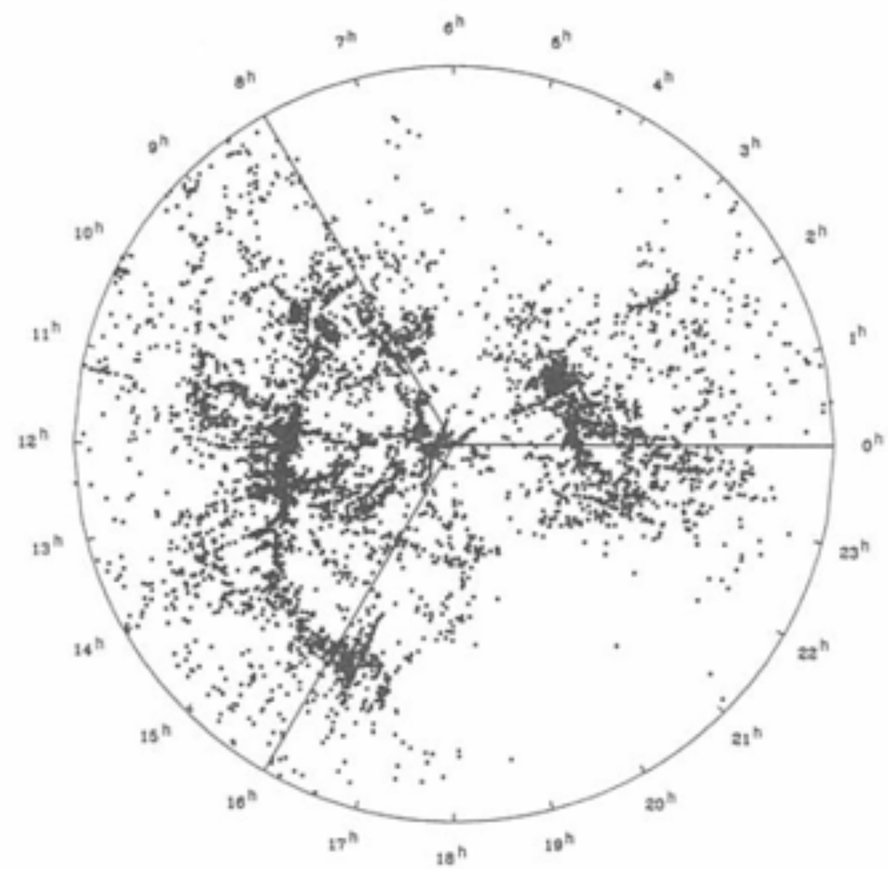

図 8.6　宇宙の大規模構造[15)]

地球から 150 h^{-1}Mpc（∼5 億光年）内の 6112 個の銀河の分布．円の中心が地球．9 時∼16 時までつらなっているのが巨大な壁（great wall）であり，泡構造なども見える．

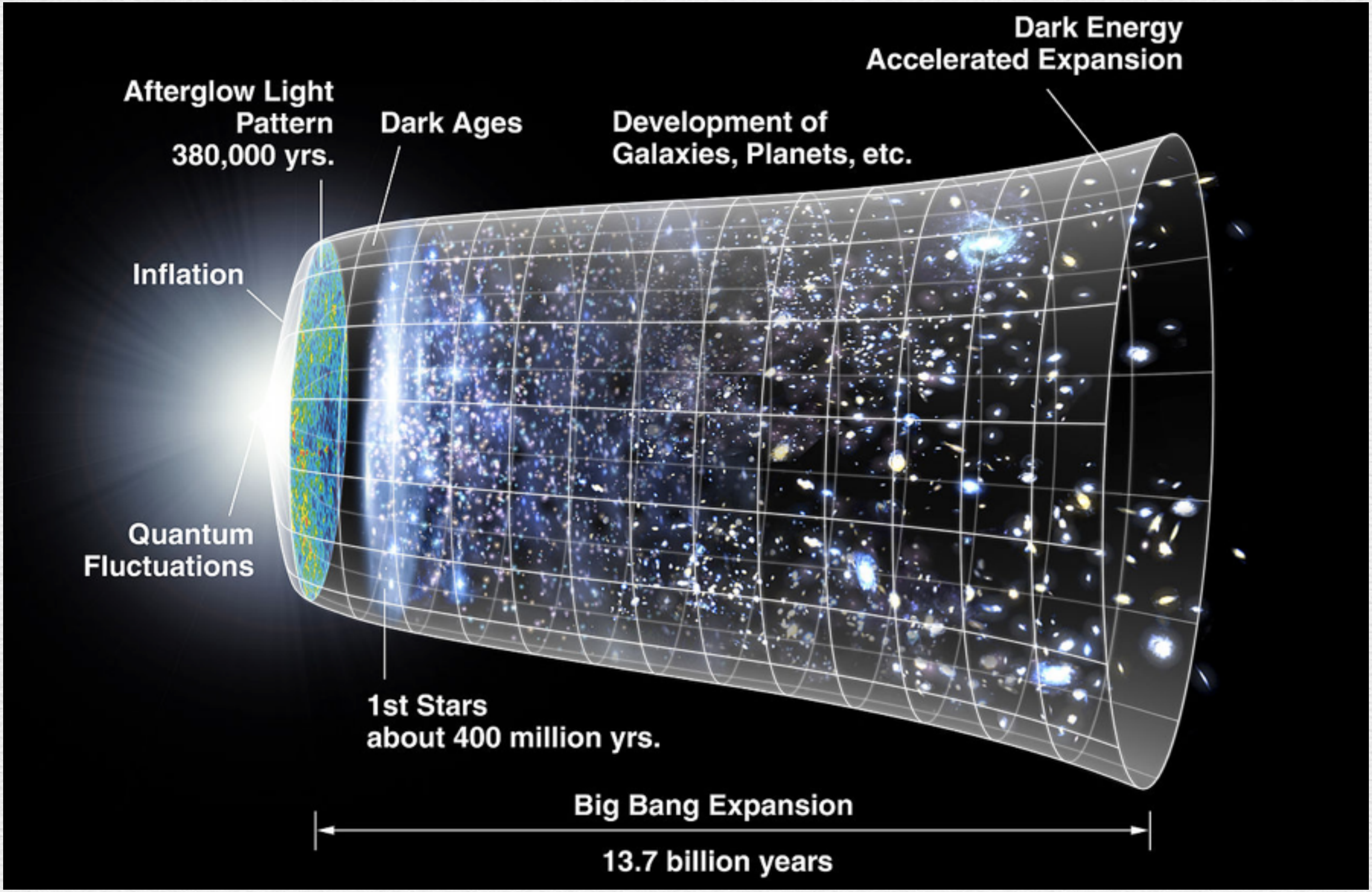

The present expansion of the universe is accelerating (1998) due to the dark energy (and possibly by the second inflation)

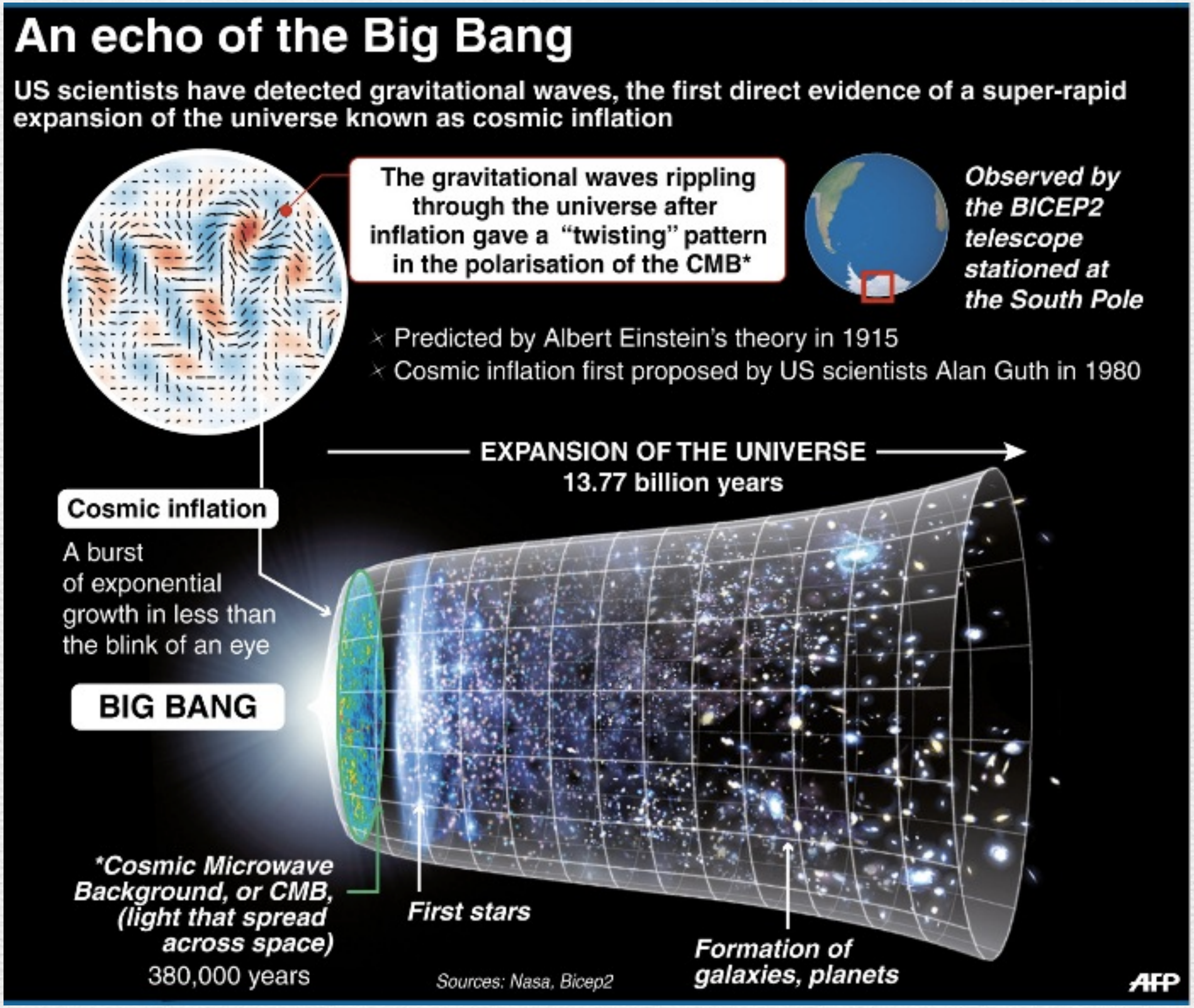
An echo of the Big Bang
US scientists have detected gravitational waves, the first direct evidence of a super-rapid expansion of the universe known as cosmic inflation
The gravitational waves rippling through the universe after inflation gave a "twisting" pattern in the polarisation of the CMB*
Observed by the BICEP2 telescope stationed at the South Pole
Predicted by Albert Einstein's theory in 1915
Cosmic inflation first proposed by US scientists Alan Guth in 1980
EXPANSION OF THE UNIVERSE
13.77 billion years
Cosmic inflation
A burst of exponential growth in less than the blink of an eye
BIG BANG
*Cosmic Microwave Background, or CMB, (light that spread across space)
380,000 years
First stars
Formation of galaxies, planets
Sources: Nasa, Bicep2
AFP

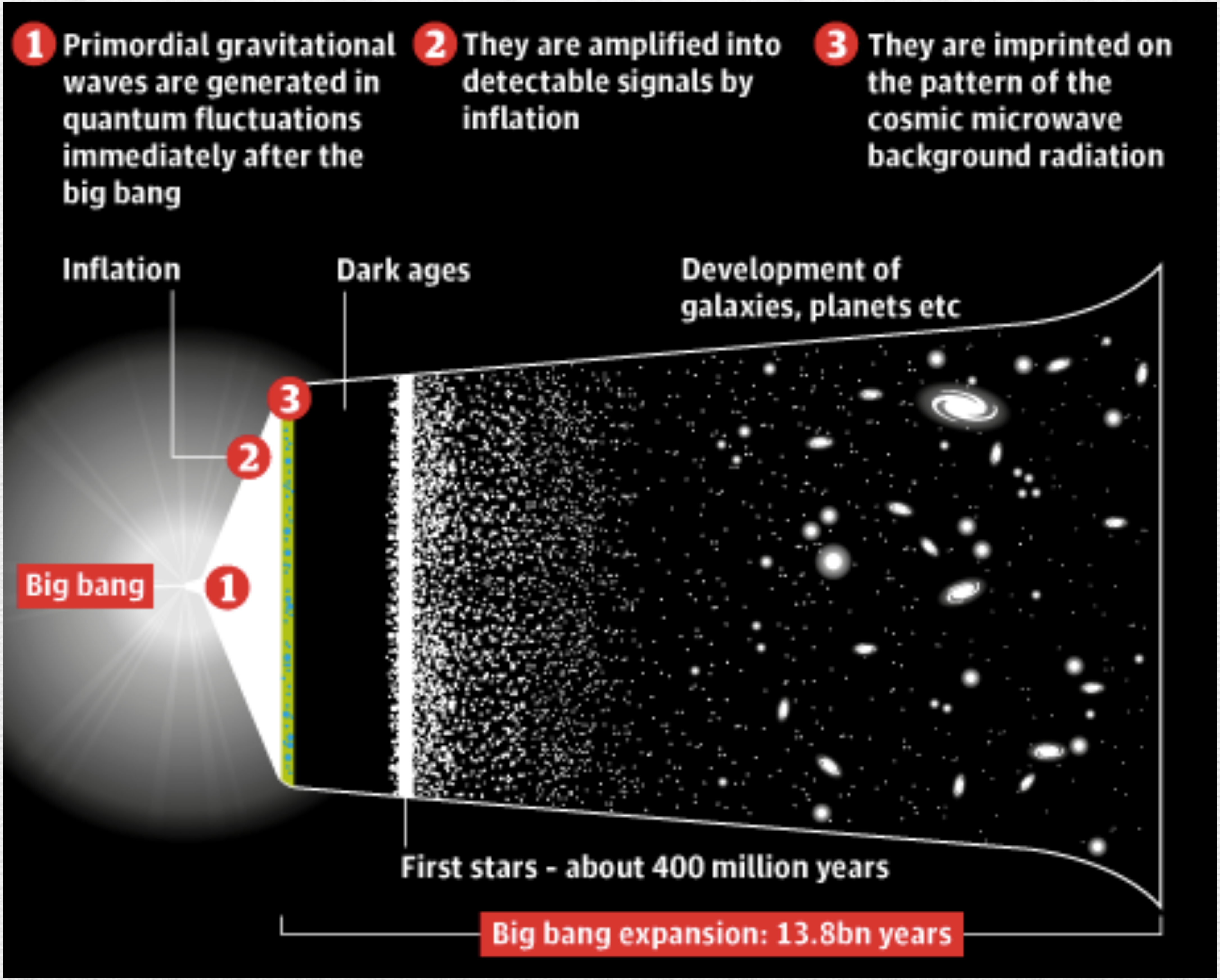

1 Primordial gravitational waves are generated in quantum fluctuations immediately after the big bang
2 They are amplified into detectable signals by inflation
3 They are imprinted on the pattern of the cosmic microwave background radiation
Inflation
Dark ages
Development of galaxies, planets etc
Big bang
1
2
3
First stars - about 400 million years
Big bang expansion: 13.8bn years

EM-Wave Polarization and Stokes Parameters

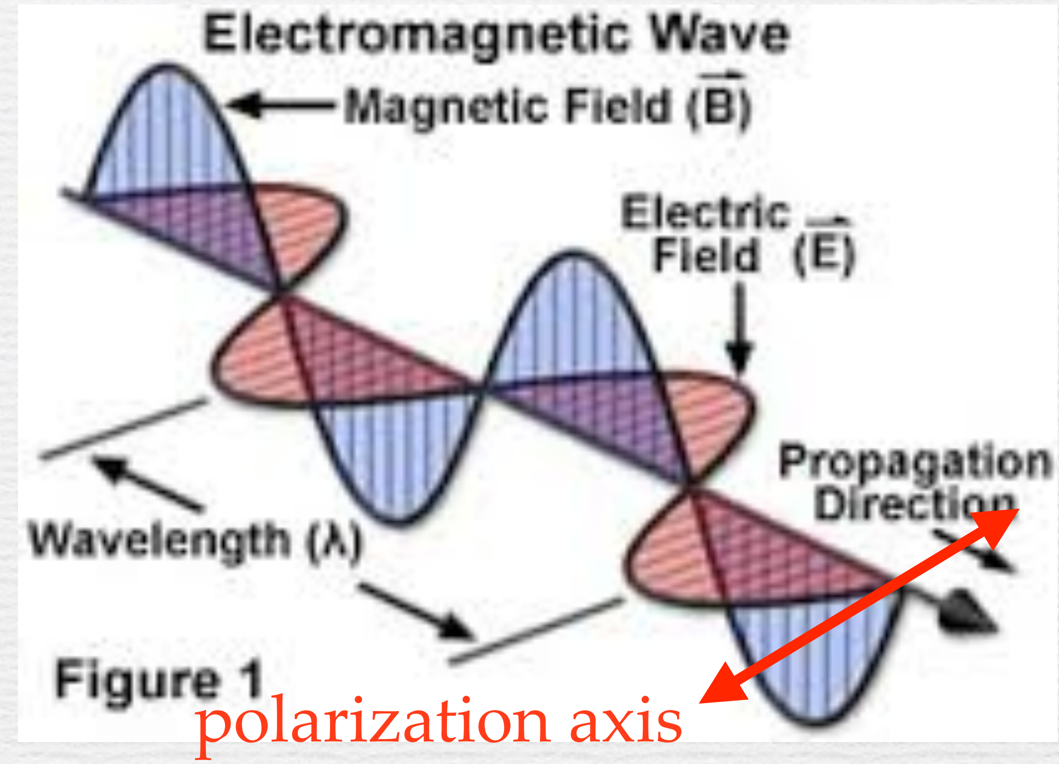

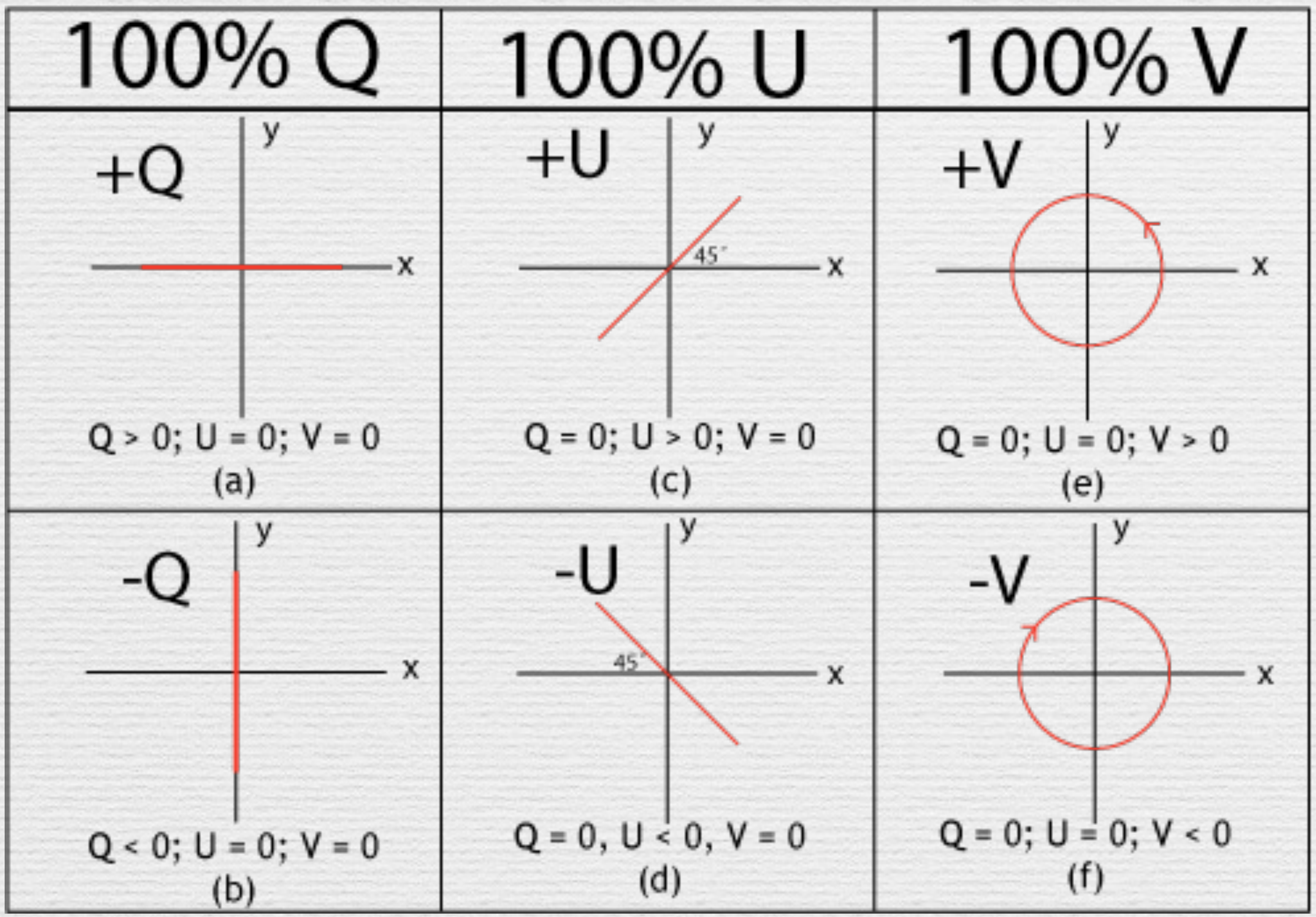

Linear polarization axis is defined in the direction of the electric oscillation of the electromagnetic wave (light).

no circular polarization in the present discussions (V=0)

Linear Polarization by Thomson Scattering

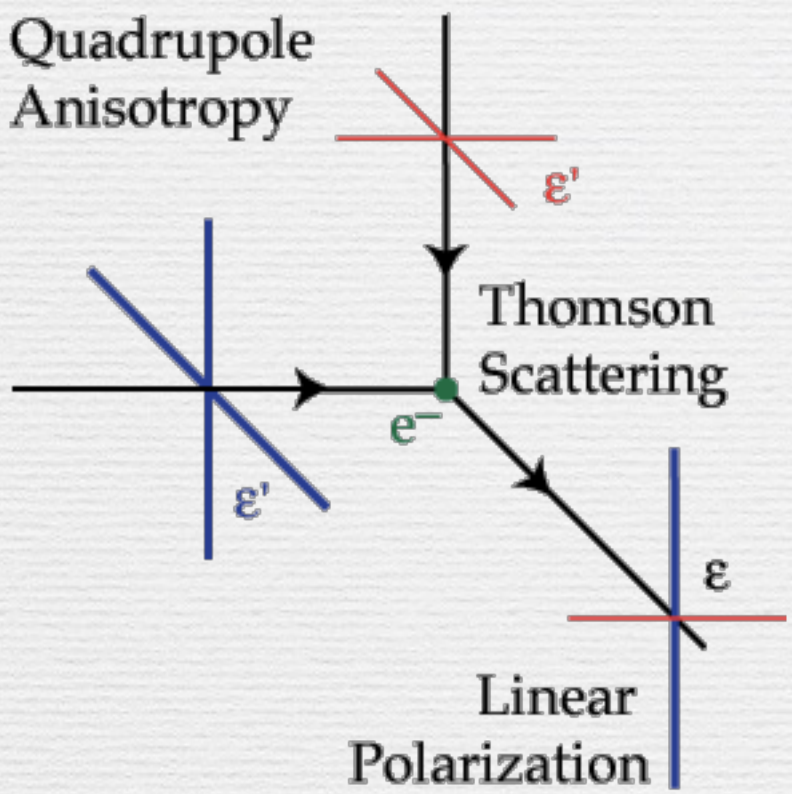

Linear Polarization: Scalar Potential

nsity inunformity

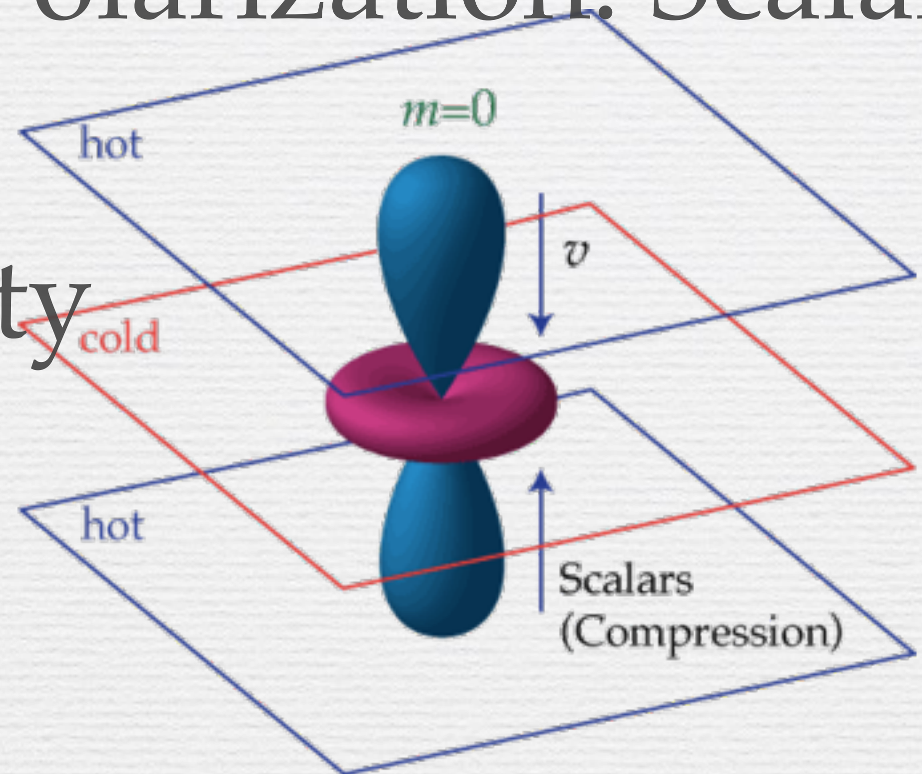

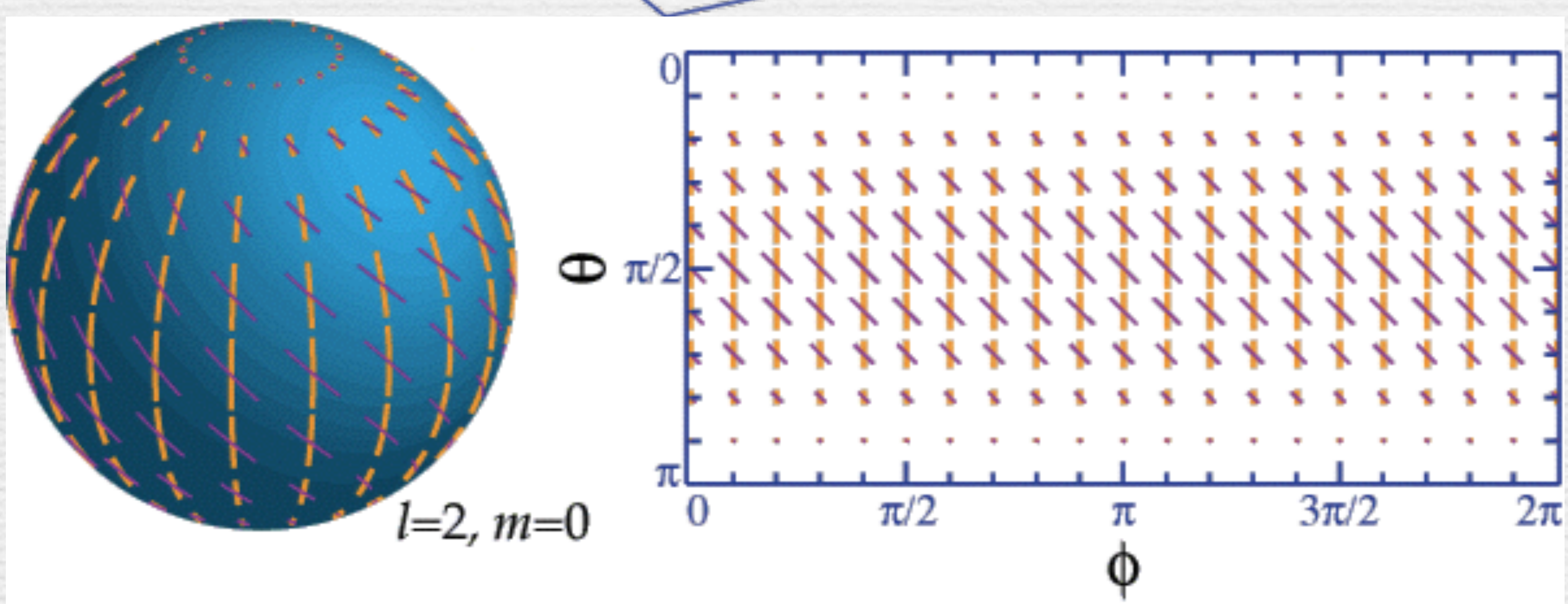

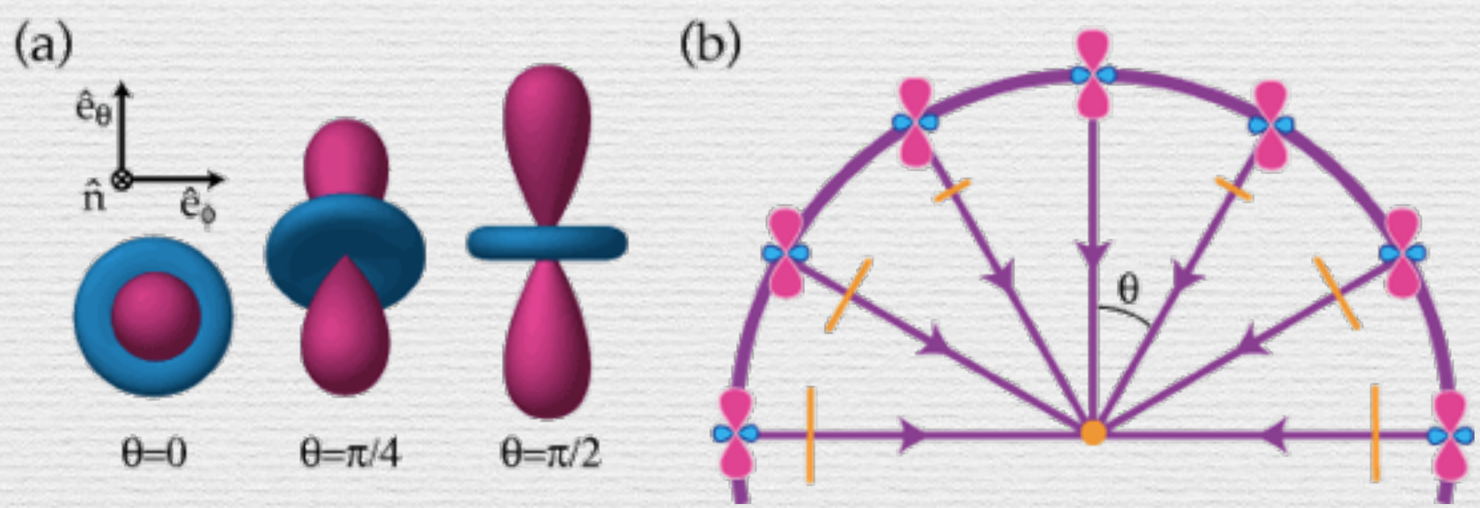

Linear Polarization: Tensor Squeeze by Gravitational Waves

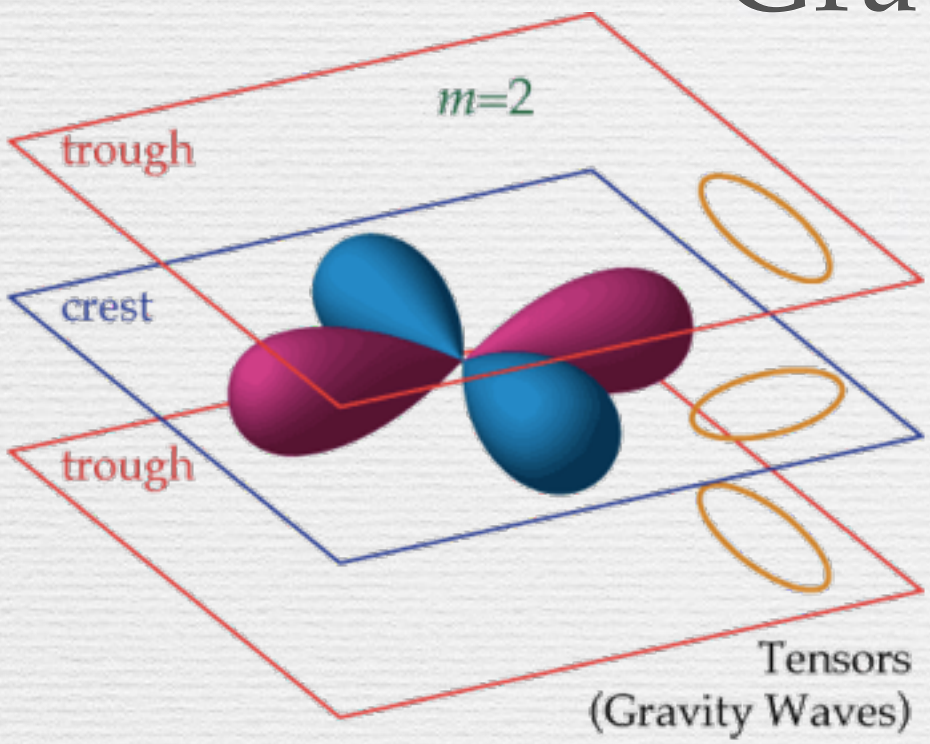

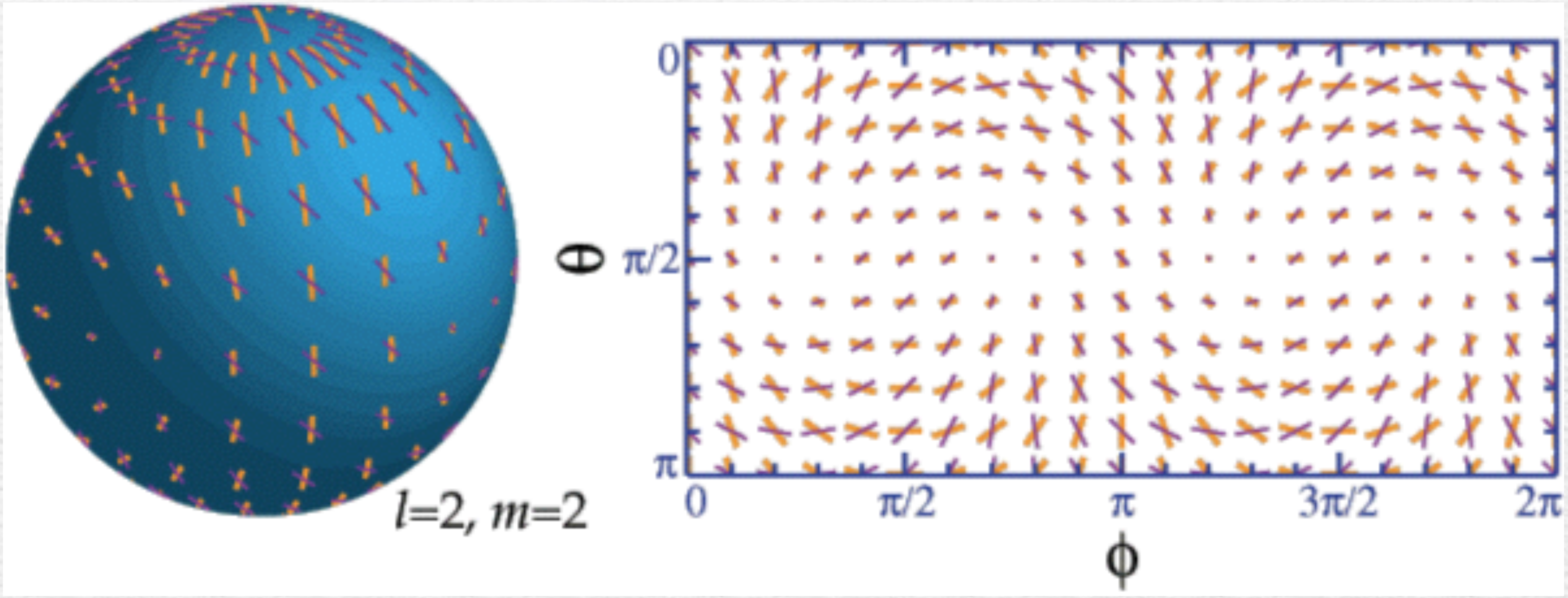

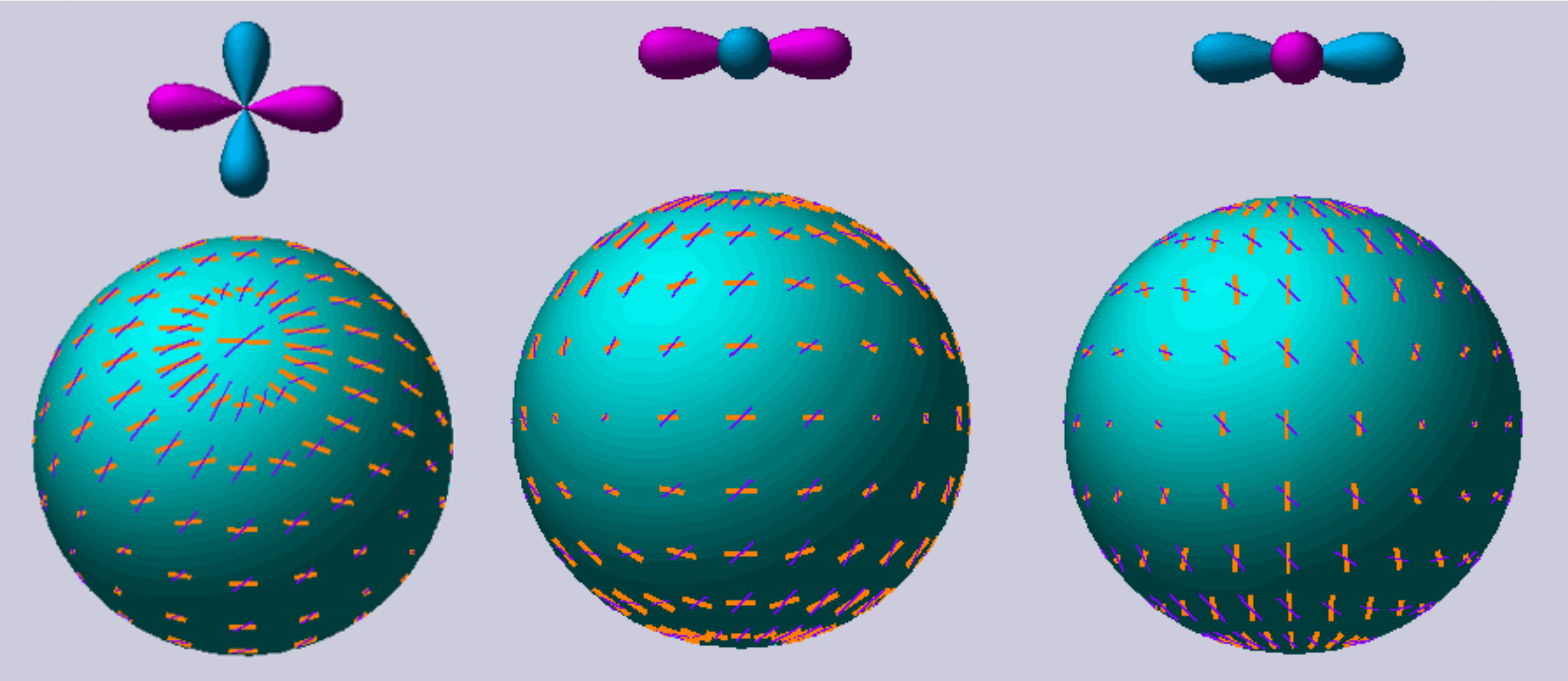

Density Perturbation (scalar)

E-mode (gradient pattern)

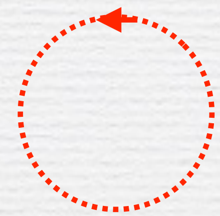

direction of the largest change of polarization

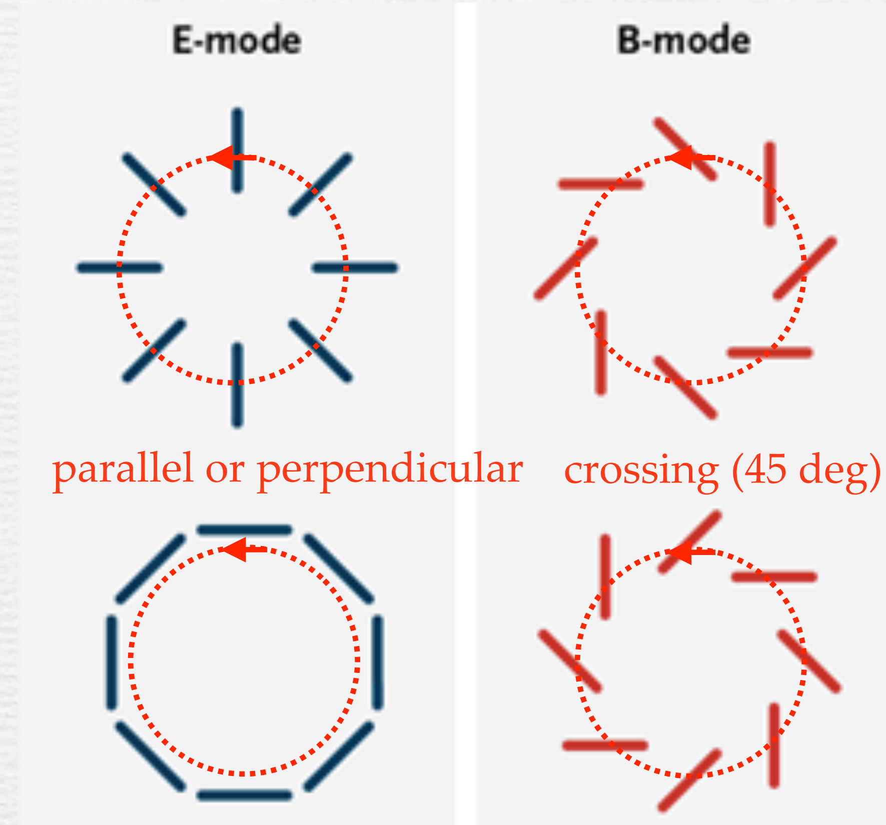

~ gradient

~ curl

Gravitational Wave (tensor)

B-mode (curl pattern)

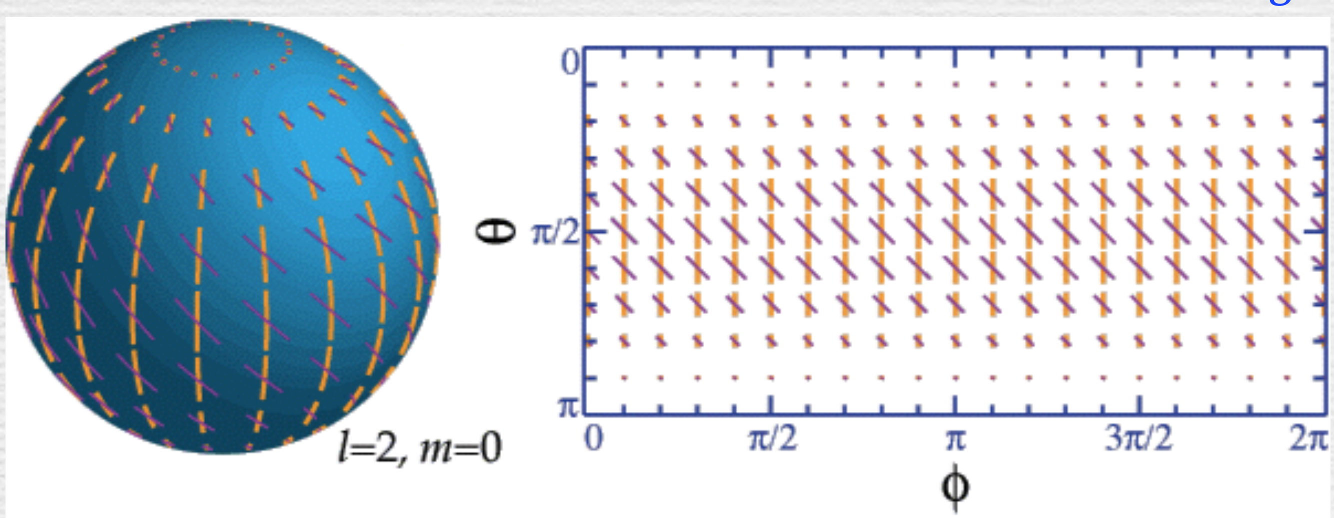

Scalar
→

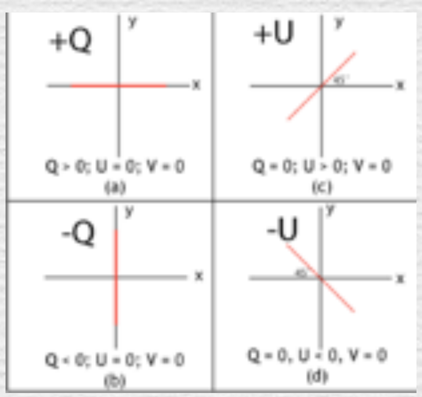

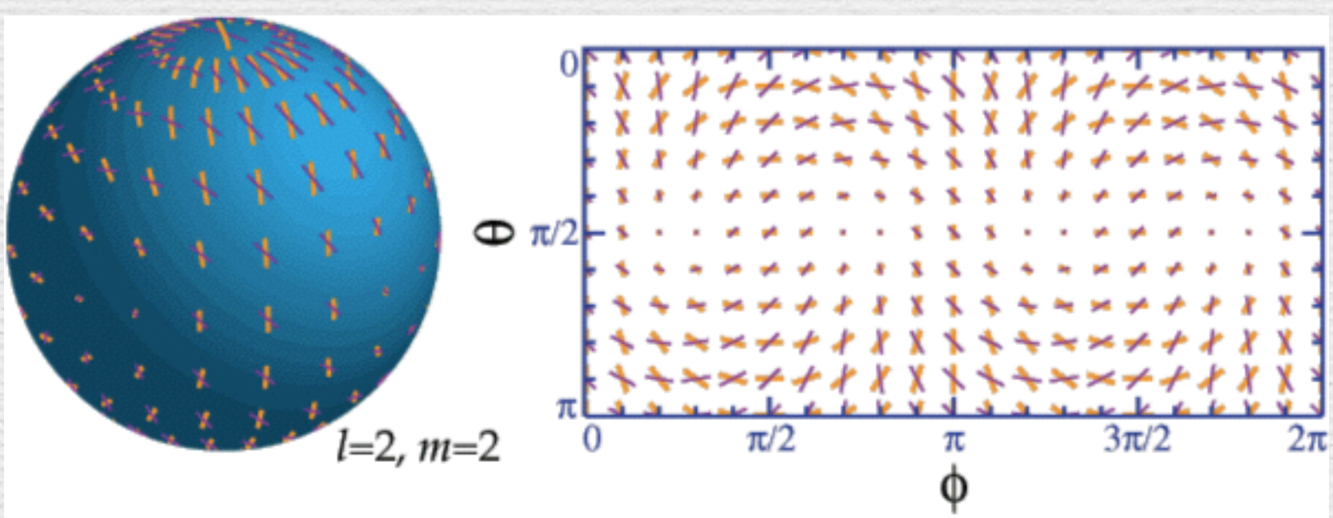

Tensor
→

Example: Plane Wave Modulation

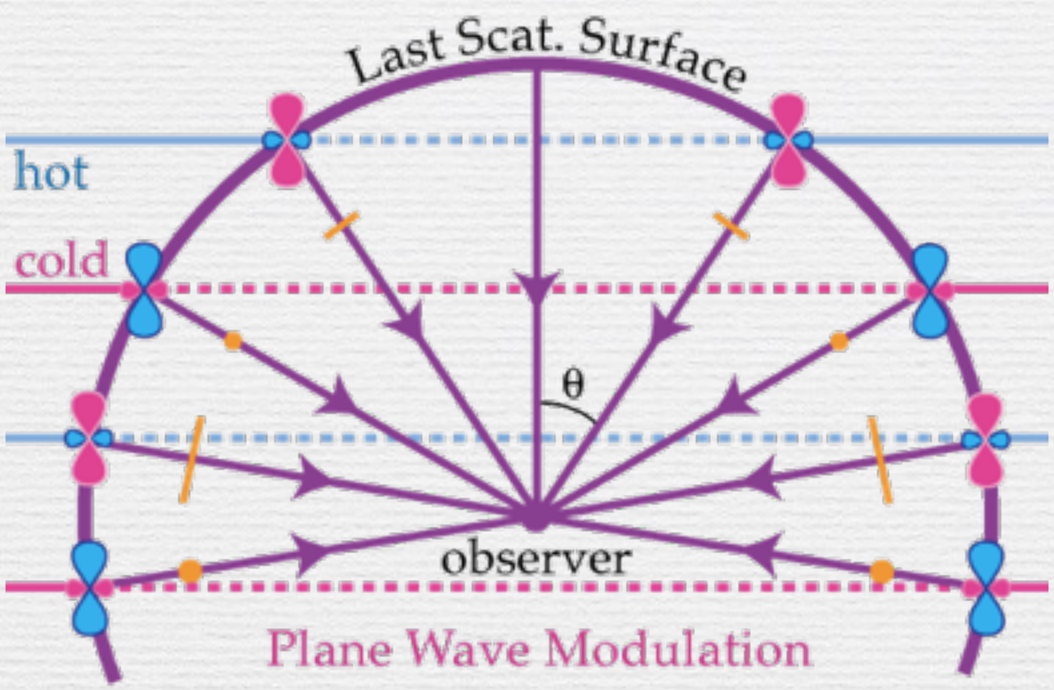

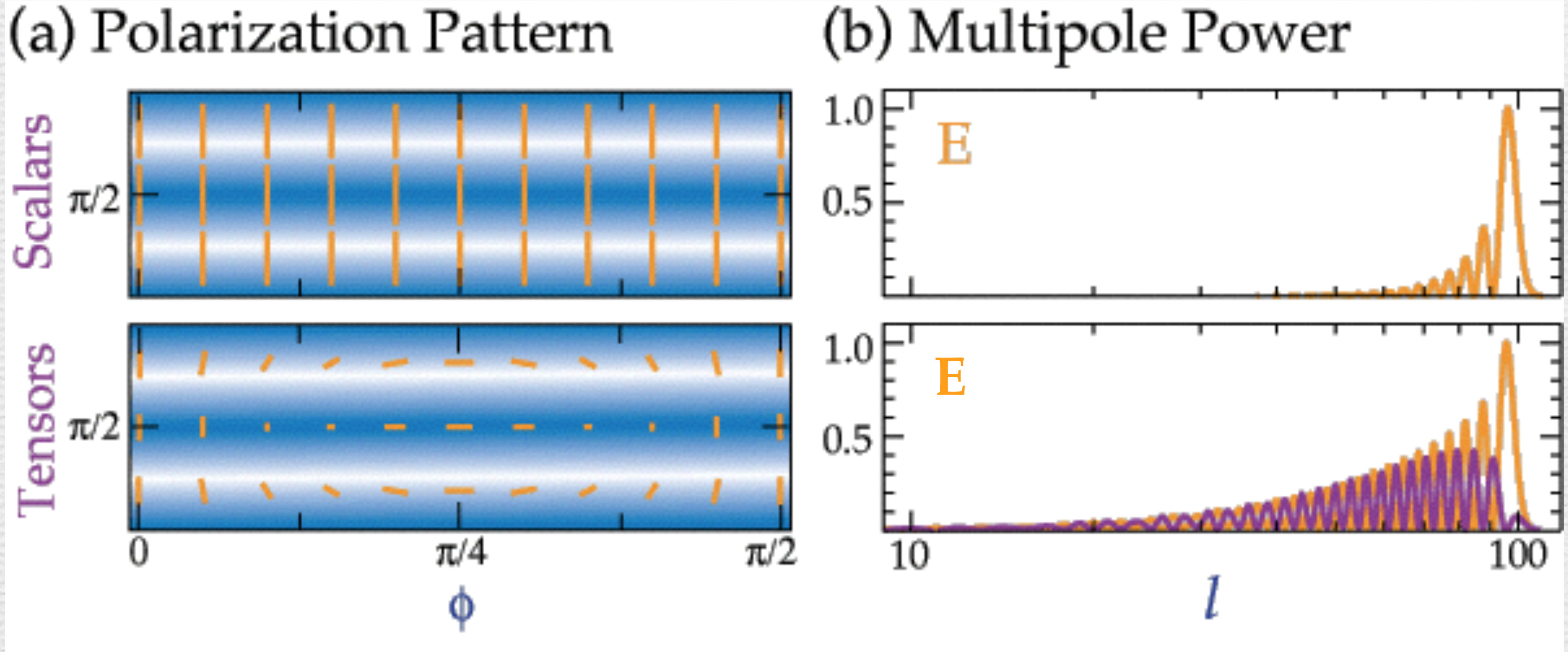

Generation of B-mode due to mixing of Q and U components

Telescope and Observation

Cosmic Background Explorer (COBE)

Nobel Prize in Physics 2006

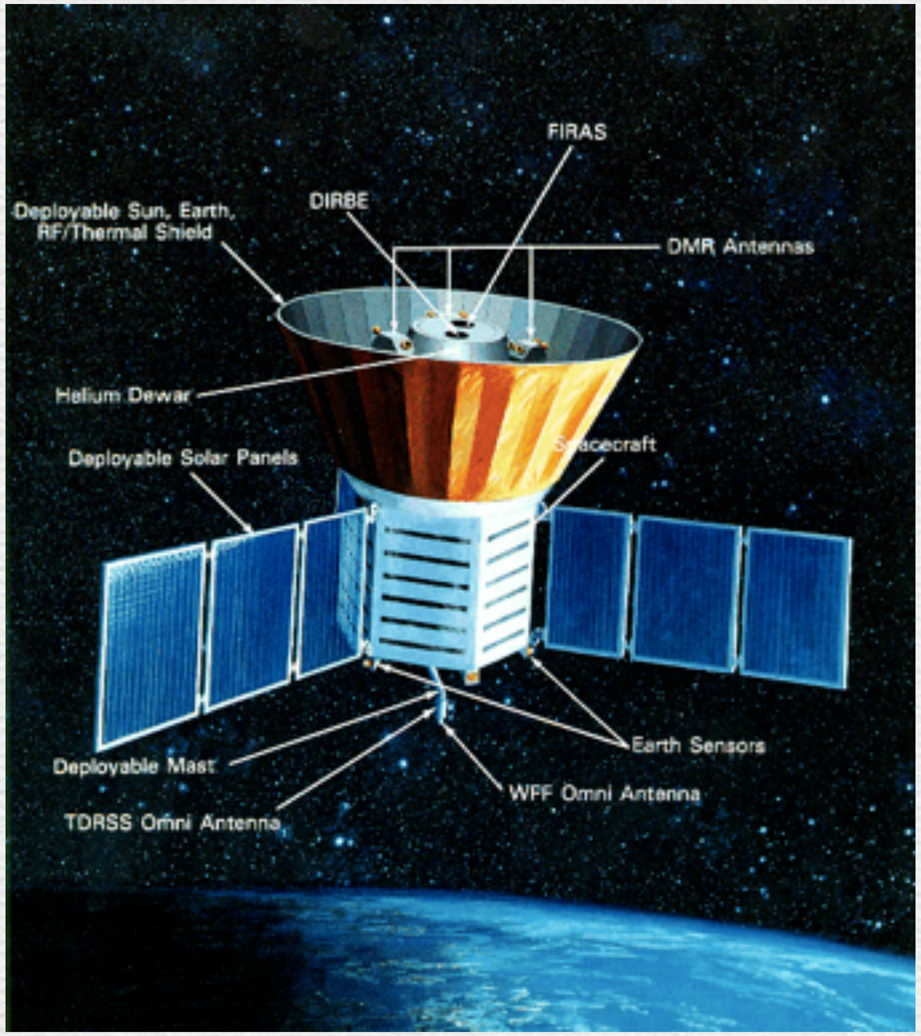

Launched on

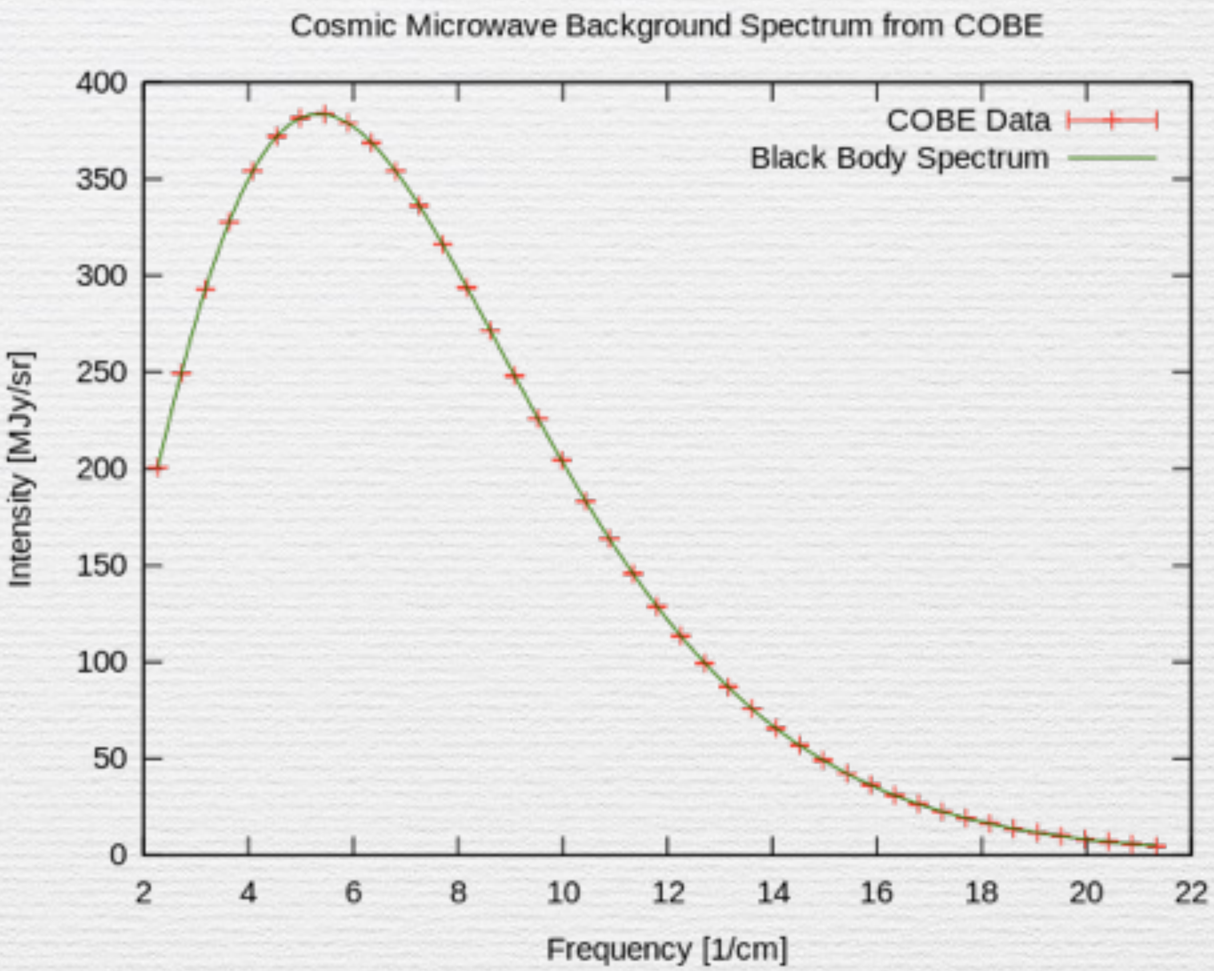

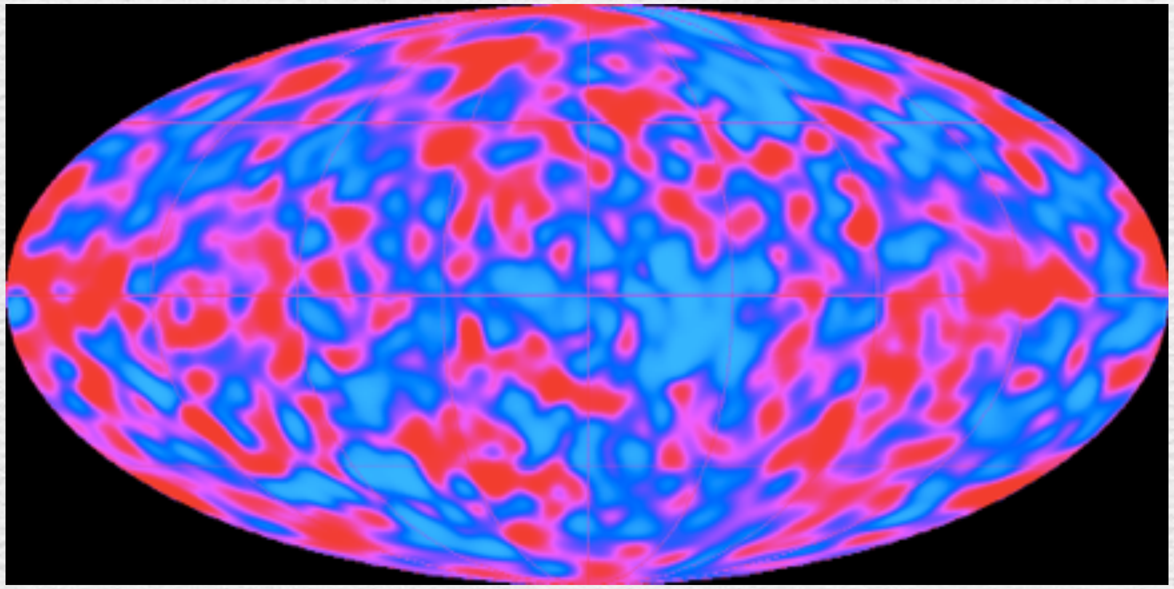

Wilkinson Microwave Anisotropy Probe (WMAP)

Launched

23, 33, 41, 61, 94 GHz

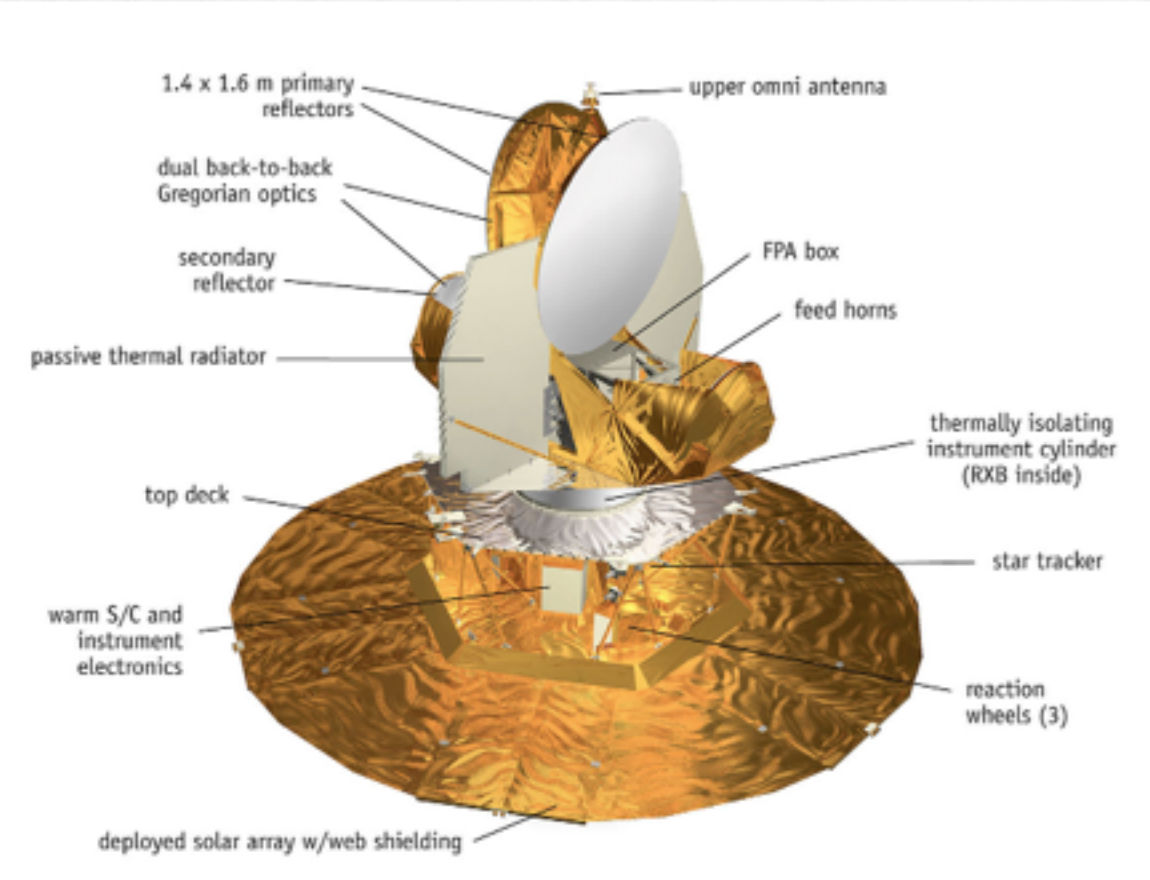

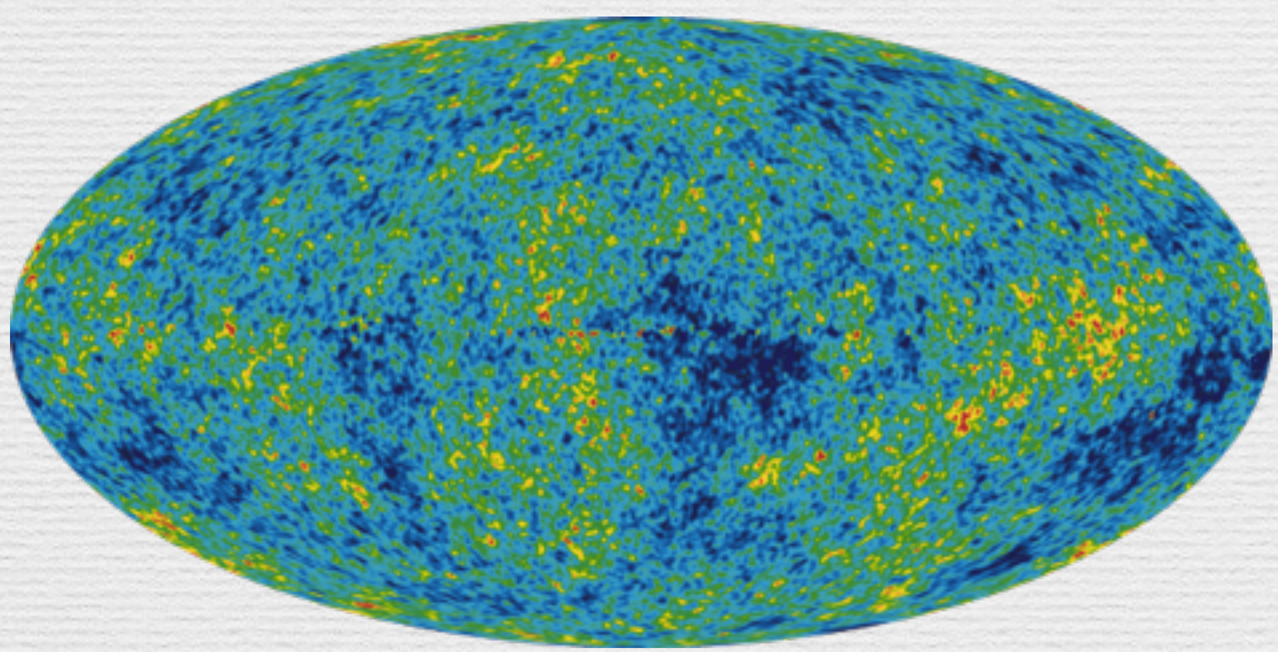

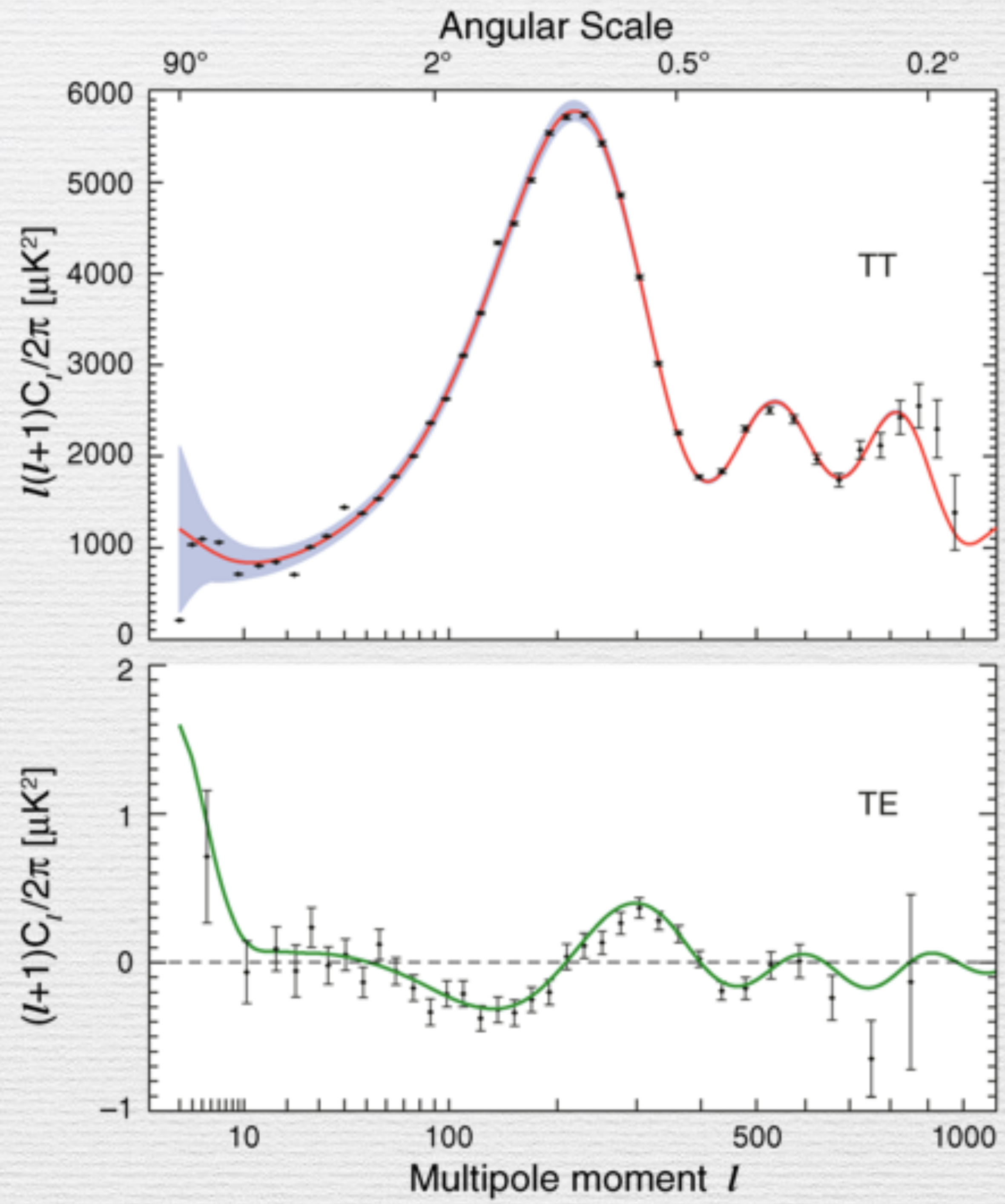

Planck

P.A.R. Ade et al., arXiv:1303.5075v2 (2013)

P.A.R. Ade et al., arXiv:1303.5076v3 (2014)

Launched on 14 May 2009

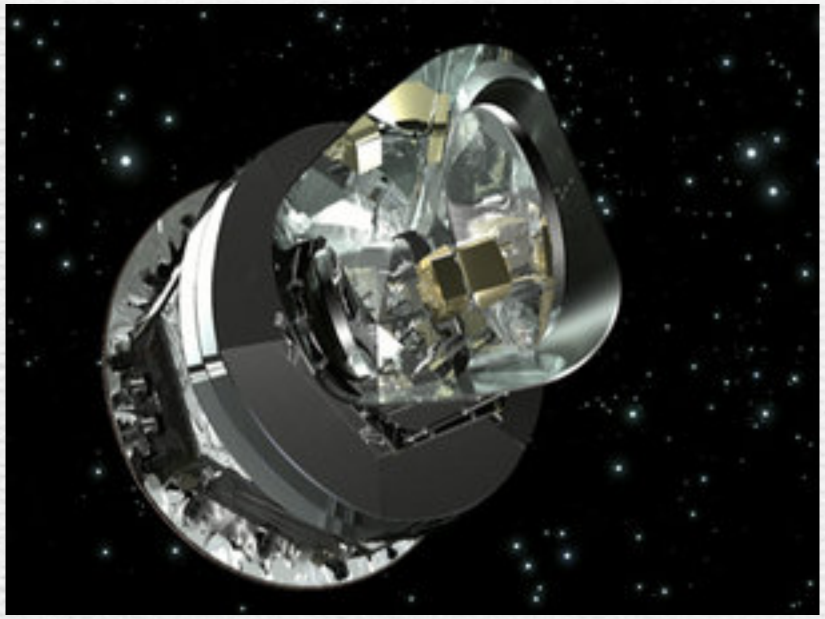

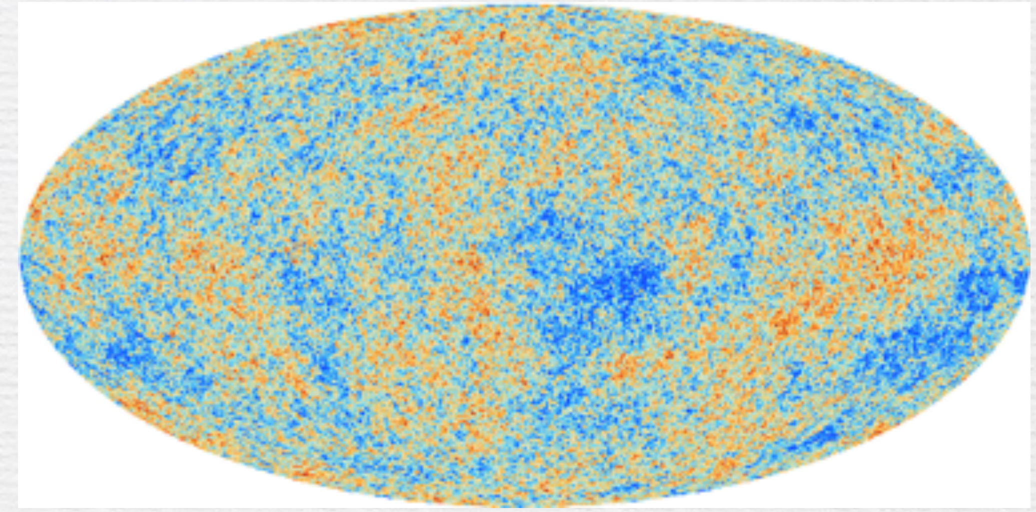

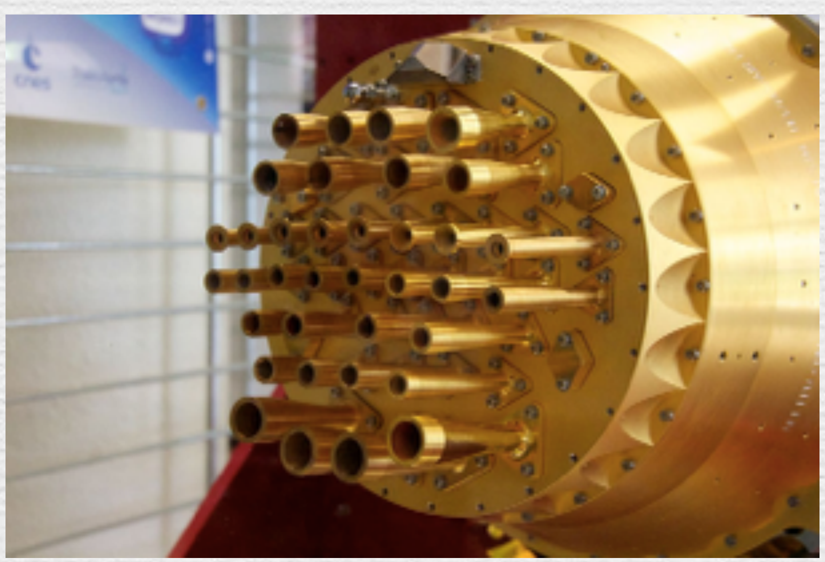

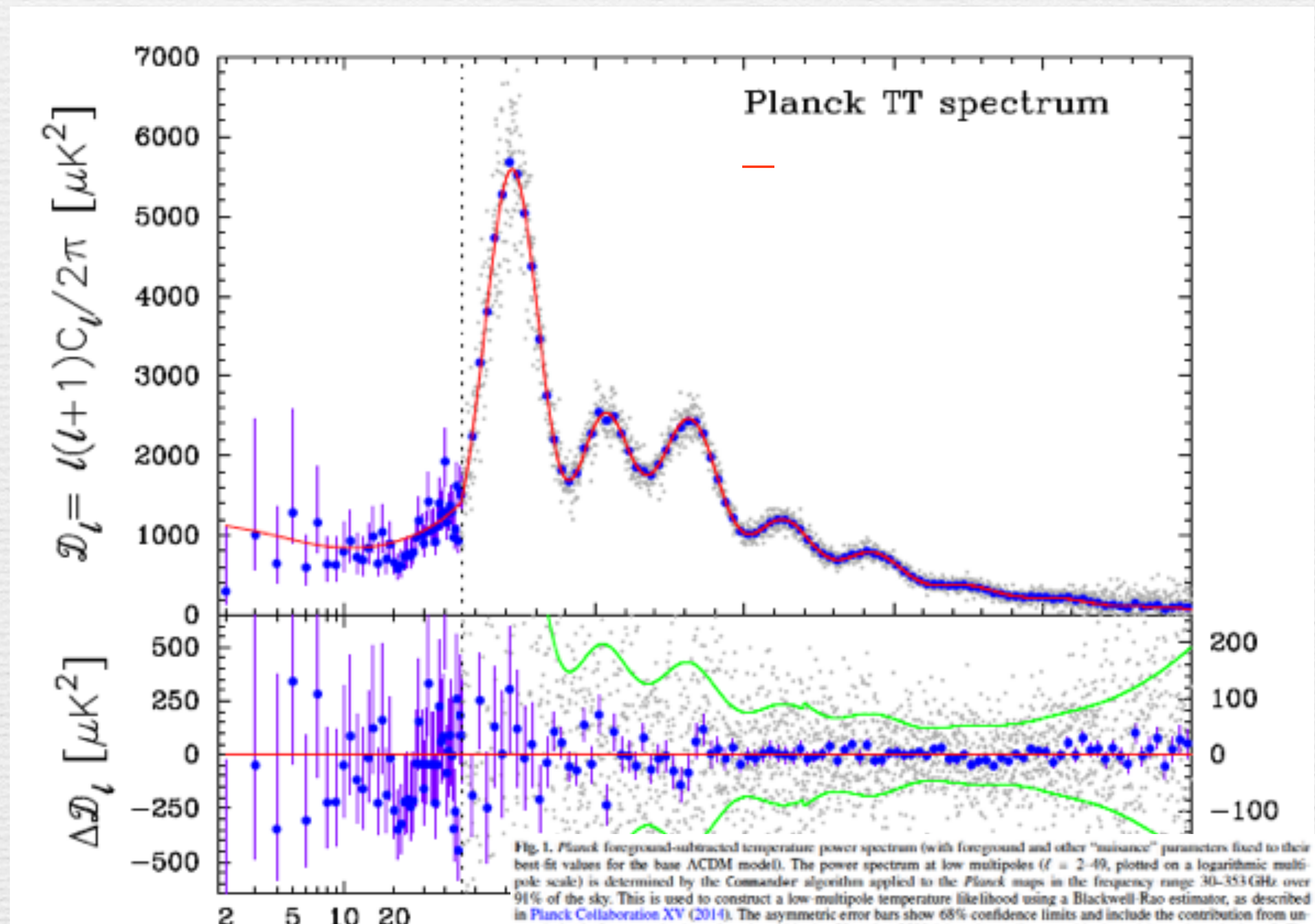

Fig. 1. *Planck* foreground-subtracted temperature power spectrum (with foreground and other "nuisance" parameters fixed to their best-fit values for the base ΛCDM model). The power spectrum at low multipoles ($\ell = 2$–49, plotted on a logarithmic multipole scale) is determined by the Commander algorithm applied to the *Planck* maps in the frequency range 30–353 GHz over 91% of the sky. This is used to construct a low-multipole temperature likelihood using a Blackwell-Rao estimator, as described in Planck Collaboration XV (2014). The asymmetric error bars show 68% confidence limits and include the contribution from uncertainties in foreground subtraction. At multipoles $50 \le \ell \le 2500$ (plotted on a linear multipole scale) we show the best-fit The CMB spectrum computed from the CamSpec likelihood (see Planck Collaboration XV 2014) after removal of unresolved foreground components. This spectrum is averaged over the frequency range 100–217 GHz using frequency-dependent diffuse sky cuts (retaining 58% of the sky at 100 GHz and 37% of the sky at 143 and 217 GHz) and is sample-variance limited to $\ell \sim 1600$. The light grey points show the power spectrum multipole by multipole. The blue points show averages in bands of width $\Delta\ell \approx 31$ together with 1σ errors computed from the diagonal components of the band-averaged covariance matrix (which includes contributions from beam and foreground uncertainties). The red line shows the temperature spectrum for the best-fit base ΛCDM cosmology. The lower panel shows the power spectrum residuals with respect to this theoretical model. The green lines show the $\pm 1\sigma$ errors on the individual power spectrum estimates at high multipoles computed from the CamSpec covariance matrix. Note the change in vertical scale in the lower panel at $\ell = 50$.

Model	Parameter	*Planck*+WP	*Planck*+WP+lensing	*Planck* + WP+high-ℓ	*Planck*+WP+BAO
ΛCDM + tensor	n_s	0.9624 ± 0.0075	0.9653 ± 0.0069	0.9600 ± 0.0071	$0.9643 + 0.0059$
	$r_{0.002}$	< 0.12	< 0.13	< 0.11	< 0.12
	$-2\Delta \ln \mathcal{L}_{max}$	0	0	0	-0.31

Table 4. Constraints on the primordial perturbation parameters in the ΛCDM+tensor model from *Planck* combined with other data sets. The constraints are given at the pivot scale $k_* = 0.002$ Mpc^{-1}.

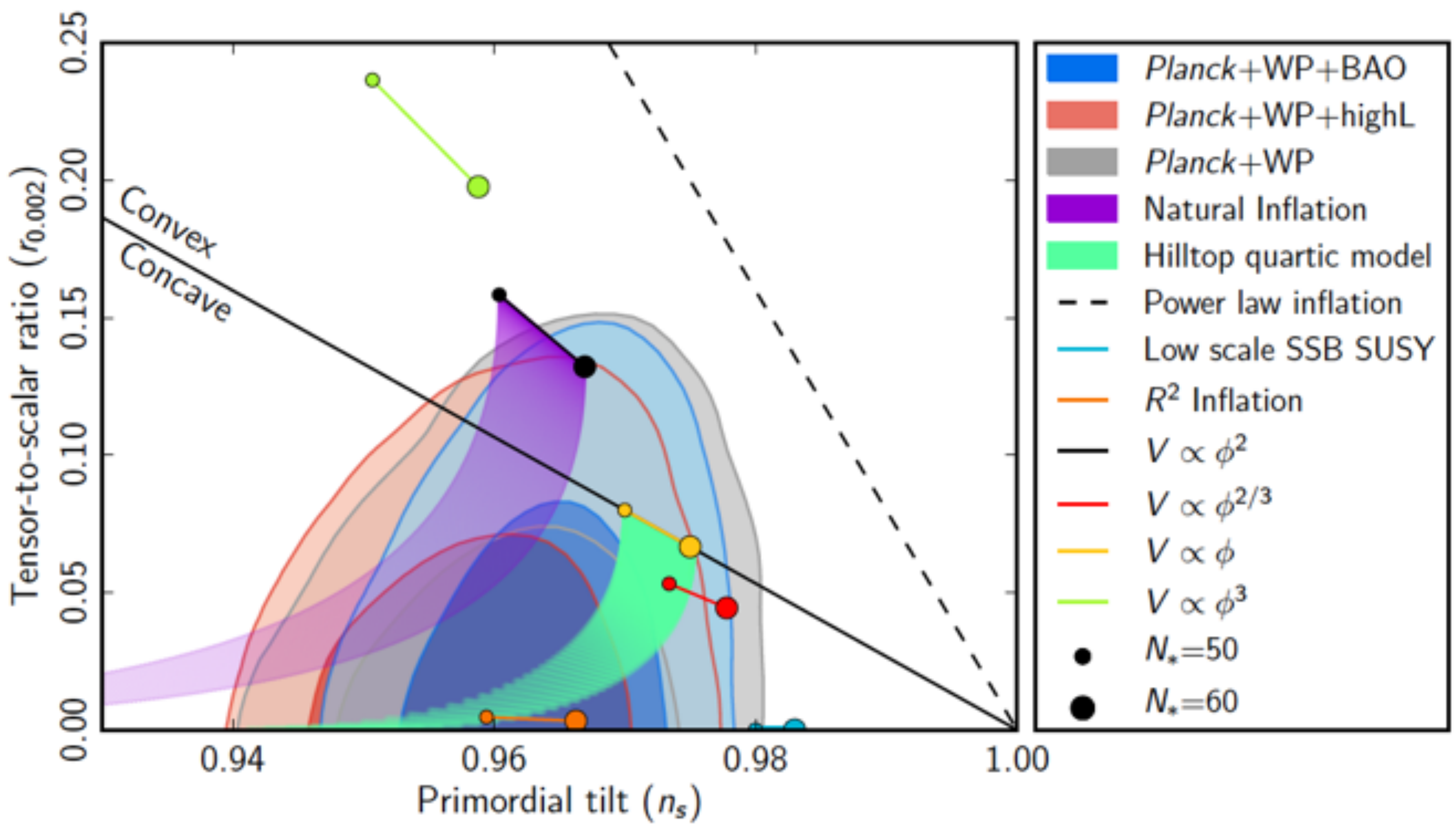

Fig. 1. Marginalized joint 68% and 95% CL regions for n_s and $r_{0.002}$ from *Planck* in combination with other data sets compared to the theoretical predictions of selected inflationary models.

Planck 2013 results. XXII. Constraints on inflation

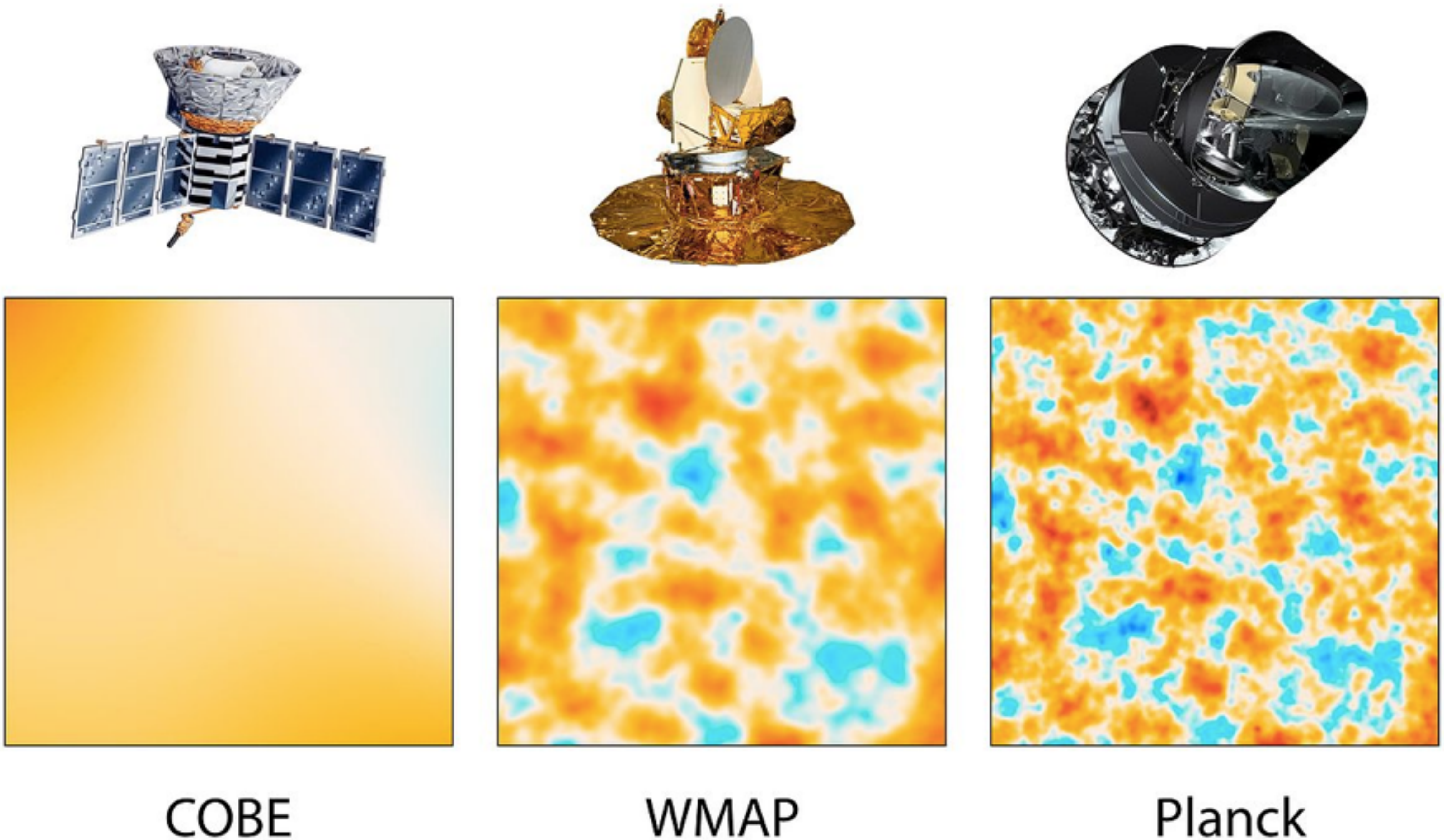
COBE
WMAP
Planck

Planck

P.A.R. Ade et al., arXiv:1303.5076v3 (2014)

Table 1. Cosmological parameters used in our analysis. For each, we give the symbol, prior range, value taken in the base ΛCDM cosmology (where appropriate), and summary definition (see text for details). The top block contains parameters with uniform priors that are varied in the MCMC chains. The ranges of these priors are listed in square brackets. The lower blocks define various derived parameters.

Parameter	Prior range	Baseline	Definition
$\omega_b \equiv \Omega_b h^2$	[0.005, 0.1]	...	Baryon density today
$\omega_c \equiv \Omega_c h^2$	[0.001, 0.99]	...	Cold dark matter density today
$100\theta_{MC}$	[0.5, 10.0]	...	100× approximation to r_*/D_A (CosmoMC)
τ	[0.01, 0.8]	...	Thomson scattering optical depth due to reionization
Ω_K	[−0.3, 0.3]	0	Curvature parameter today with $\Omega_{tot} = 1 - \Omega_K$
$\sum m_\nu$	[0, 5]	0.06	The sum of neutrino masses in eV
$m^{eff}_{\nu,\,sterile}$	[0, 3]	0	Effective mass of sterile neutrino in eV
w_0	[−3.0, −0.3]	−1	Dark energy equation of state[a], $w(a) = w_0 + (1-a)w_a$
w_a	[−2, 2]	0	As above (perturbations modelled using PPF)
N_{eff}	[0.05, 10.0]	3.046	Effective number of neutrino-like relativistic degrees of freedom (see text)
Y_P	[0.1, 0.5]	BBN	Fraction of baryonic mass in helium
A_L	[0, 10]	1	Amplitude of the lensing power relative to the physical value
n_s	[0.9, 1.1]	...	Scalar spectrum power-law index ($k_0 = 0.05\mathrm{Mpc}^{-1}$)
n_t	$n_t = -r_{0.05}/8$	Inflation	Tensor spectrum power-law index ($k_0 = 0.05\mathrm{Mpc}^{-1}$)
$dn_s/d\ln k$	[−1, 1]	0	Running of the spectral index
$\ln(10^{10}A_s)$	[2.7, 4.0]	...	Log power of the primordial curvature perturbations ($k_0 = 0.05\,\mathrm{Mpc}^{-1}$)
$r_{0.05}$	[0, 2]	0	Ratio of tensor primordial power to curvature power at $k_0 = 0.05\,\mathrm{Mpc}^{-1}$
Ω_Λ		...	Dark energy density divided by the critical density today
t_0		...	Age of the Universe today (in Gyr)
Ω_m		...	Matter density (inc. massive neutrinos) today divided by the critical density
σ_8		...	RMS matter fluctuations today in linear theory
z_{re}		...	Redshift at which Universe is half reionized
H_0	[20,100]	...	Current expansion rate in $\mathrm{km\,s^{-1}Mpc^{-1}}$
$r_{0.002}$		0	Ratio of tensor primordial power to curvature power at $k_0 = 0.002\,\mathrm{Mpc}^{-1}$
$10^9 A_s$		...	$10^9\times$ dimensionless curvature power spectrum at $k_0 = 0.05\,\mathrm{Mpc}^{-1}$
$\omega_m \equiv \Omega_m h^2$		...	Total matter density today (inc. massive neutrinos)
z_*		...	Redshift for which the optical depth equals unity (see text)
$r_* = r_s(z_*)$		...	Comoving size of the sound horizon at $z = z_*$
$100\theta_*$		...	100× angular size of sound horizon at $z = z_*$ (r_*/D_A)
z_{drag}		...	Redshift at which baryon-drag optical depth equals unity (see text)
$r_{drag} = r_s(z_{drag})$		...	Comoving size of the sound horizon at $z = z_{drag}$
k_D		...	Characteristic damping comoving wavenumber (Mpc^{-1})
$100\theta_D$		...	100× angular extent of photon diffusion at last scattering (see text)
z_{eq}		...	Redshift of matter-radiation equality (massless neutrinos)
$100\theta_{eq}$		...	100× angular size of the comoving horizon at matter-radiation equality
$r_{drag}/D_V(0.57)$		...	BAO distance ratio at $z = 0.57$ (see Sect. 5.2)

[a] For dynamical dark energy models with constant equation of state, we denote the equation of state by w and adopt the same prior as for w_0.

Table 2. Cosmological parameter values for the six-parameter base ΛCDM model. Columns 2 and 3 give results for the *Planck* temperature power spectrum data alone. Columns 4 and 5 combine the *Planck* temperature data with *Planck* lensing, and columns 6 and 7 include *WMAP* polarization at low multipoles. We give best fit parameters (i.e. the parameters that maximise the overall likelihood for each data combination) as well as 68% confidence limits for constrained parameters. The first six parameters have flat priors. The remainder are derived parameters as discussed in Sect. 2. Beam, calibration parameters, and foreground parameters (see Sect. 4) are not listed for brevity. Constraints on foreground parameters for *Planck*+WP are given later in Table 5.

	Planck		*Planck*+lensing		*Planck*+WP	
Parameter	Best fit	68% limits	Best fit	68% limits	Best fit	68% limits
$\Omega_b h^2$	0.022068	0.02207 ± 0.00033	0.022242	0.02217 ± 0.00033	0.022032	0.02205 ± 0.00028
$\Omega_c h^2$	0.12029	0.1196 ± 0.0031	0.11805	0.1186 ± 0.0031	0.12038	0.1199 ± 0.0027
$100\theta_{MC}$	1.04122	1.04132 ± 0.00068	1.04150	1.04141 ± 0.00067	1.04119	1.04131 ± 0.00063
τ	0.0925	0.097 ± 0.038	0.0949	0.089 ± 0.032	0.0925	$0.089^{+0.012}_{-0.014}$
n_s	0.9624	0.9616 ± 0.0094	0.9675	0.9635 ± 0.0094	0.9619	0.9603 ± 0.0073
$\ln(10^{10}A_s)$	3.098	3.103 ± 0.072	3.098	3.085 ± 0.057	3.0980	$3.089^{+0.024}_{-0.027}$
Ω_Λ	0.6825	0.686 ± 0.020	0.6964	0.693 ± 0.019	0.6817	$0.685^{+0.018}_{-0.016}$
Ω_m	0.3175	0.314 ± 0.020	0.3036	0.307 ± 0.019	0.3183	$0.315^{+0.016}_{-0.018}$
σ_8	0.8344	0.834 ± 0.027	0.8285	0.823 ± 0.018	0.8347	0.829 ± 0.012
z_{re}	11.35	$11.4^{+4.0}_{-2.8}$	11.45	$10.8^{+3.1}_{-2.5}$	11.37	11.1 ± 1.1
H_0	67.11	67.4 ± 1.4	68.14	67.9 ± 1.5	67.04	67.3 ± 1.2
$10^9 A_s$	2.215	2.23 ± 0.16	2.215	$2.19^{+0.12}_{-0.14}$	2.215	$2.196^{+0.051}_{-0.060}$
$\Omega_m h^2$	0.14300	0.1423 ± 0.0029	0.14094	0.1414 ± 0.0029	0.14305	0.1426 ± 0.0025
$\Omega_m h^3$	0.09597	0.09590 ± 0.00059	0.09603	0.09593 ± 0.00058	0.09591	0.09589 ± 0.00057
Y_P	0.247710	0.24771 ± 0.00014	0.247785	0.24775 ± 0.00014	0.247695	0.24770 ± 0.00012
Age/Gyr	13.819	13.813 ± 0.058	13.784	13.796 ± 0.058	13.8242	13.817 ± 0.048
z_*	1090.43	1090.37 ± 0.65	1090.01	1090.16 ± 0.65	1090.48	1090.43 ± 0.54
r_*	144.58	144.75 ± 0.66	145.02	144.96 ± 0.66	144.58	144.71 ± 0.60
$100\theta_*$	1.04139	1.04148 ± 0.00066	1.04164	1.04156 ± 0.00066	1.04136	1.04147 ± 0.00062
z_{drag}	1059.32	1059.29 ± 0.65	1059.59	1059.43 ± 0.64	1059.25	1059.25 ± 0.58
r_{drag}	147.34	147.53 ± 0.64	147.74	147.70 ± 0.63	147.36	147.49 ± 0.59
k_D	0.14026	0.14007 ± 0.00064	0.13998	0.13996 ± 0.00062	0.14022	0.14009 ± 0.00063
$100\theta_D$	0.161332	0.16137 ± 0.00037	0.161196	0.16129 ± 0.00036	0.161375	0.16140 ± 0.00034
z_{eq}	3402	3386 ± 69	3352	3362 ± 69	3403	3391 ± 60
$100\theta_{eq}$	0.8128	0.816 ± 0.013	0.8224	0.821 ± 0.013	0.8125	0.815 ± 0.011
$r_{drag}/D_V(0.57)$	0.07130	0.0716 ± 0.0011	0.07207	0.0719 ± 0.0011	0.07126	0.07147 ± 0.00091

BICEP1

Y.D. Takahashi et al., Astrophy. J., 711:1141–1156, 2010

M. Su et al., Astrophy. J., 783:67, 201

Year 2006-2008

Neutron transmutation doped (NTD) germanium thermistor bolometer

100, 150, and 220 GHz

r < 0.65 at 95% CL.

ΛCDM model = "standard" cosmological model with cosmological constant (Λ

r = tensor to scalar ratio of the fluctuation

The BICEP1 result and comparison with ΛCDM model with r=0.1.

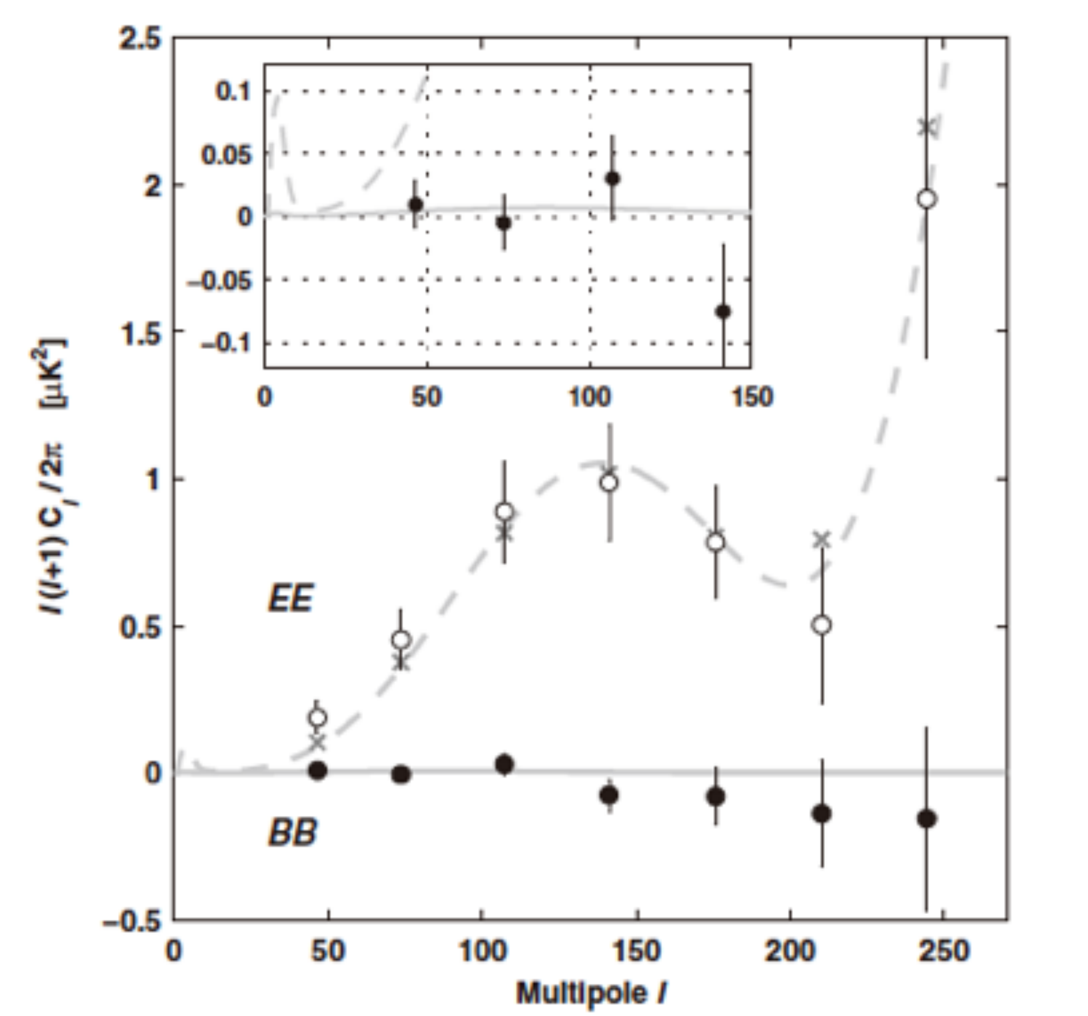

Figure 9. Close-up of the *EE* and *BB* spectra from Figure 5. BICEP1 measures *EE* polarization (open circles) with high signal-to-noise ratio at degree angular scales (Section 9.2). The *BB* spectrum (black points) is consistent with zero. Theoretical *BB* and *EE* spectra with $r = 0.1$ are shown in solid and dashed gray lines, respectively. The gray crosses are the band power expectation value for the *EE* spectrum. They diverge from the ΛCDM curve because of the detailed shape of the band power window functions. The inset shows the low-ℓ region in more detail.

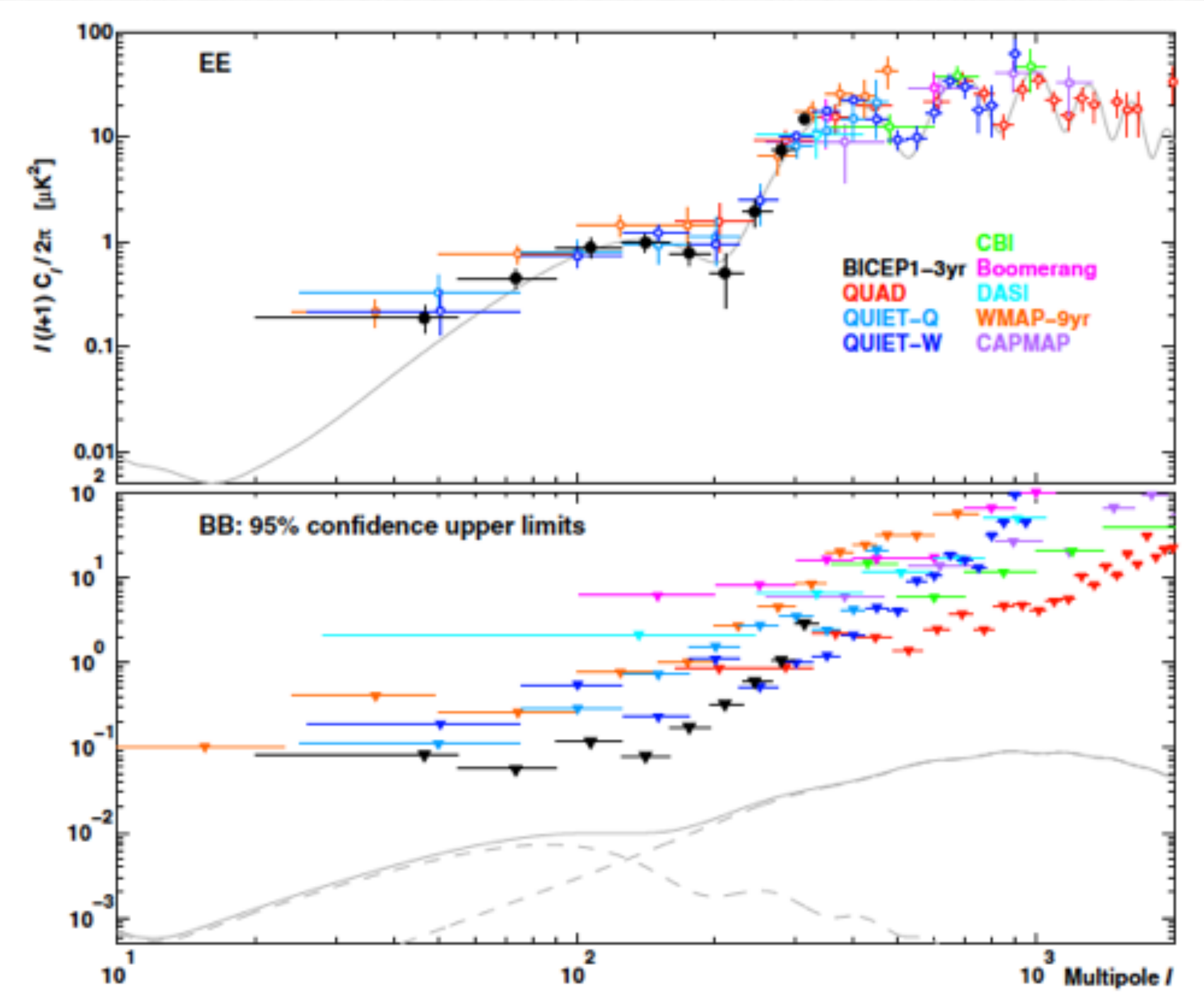

Figure 13. BICEP1's *EE* and *BB* power spectra complement existing data from other CMB polarization experiments (Leitch et al. 2005; Montroy et al. 2006; Sievers et al. 2007; Bischoff et al. 2008; Brown et al. 2009; QUIET Collaboration et al. 2011, 2012; Bennett et al. 2013). For visual clarity, we only display the experiments where at least one of the *EE* band powers has a center value that is greater than twice the distance between the center value and the lower end of the 68% confidence interval. Theoretical spectra from a ΛCDM model with $r = 0.1$ are shown for comparison; the *BB* curve is the sum of the inflationary and gravitational lensing components. At degree angular scales, BICEP1's constraints on *BB* are the most powerful to date.

BICEP2

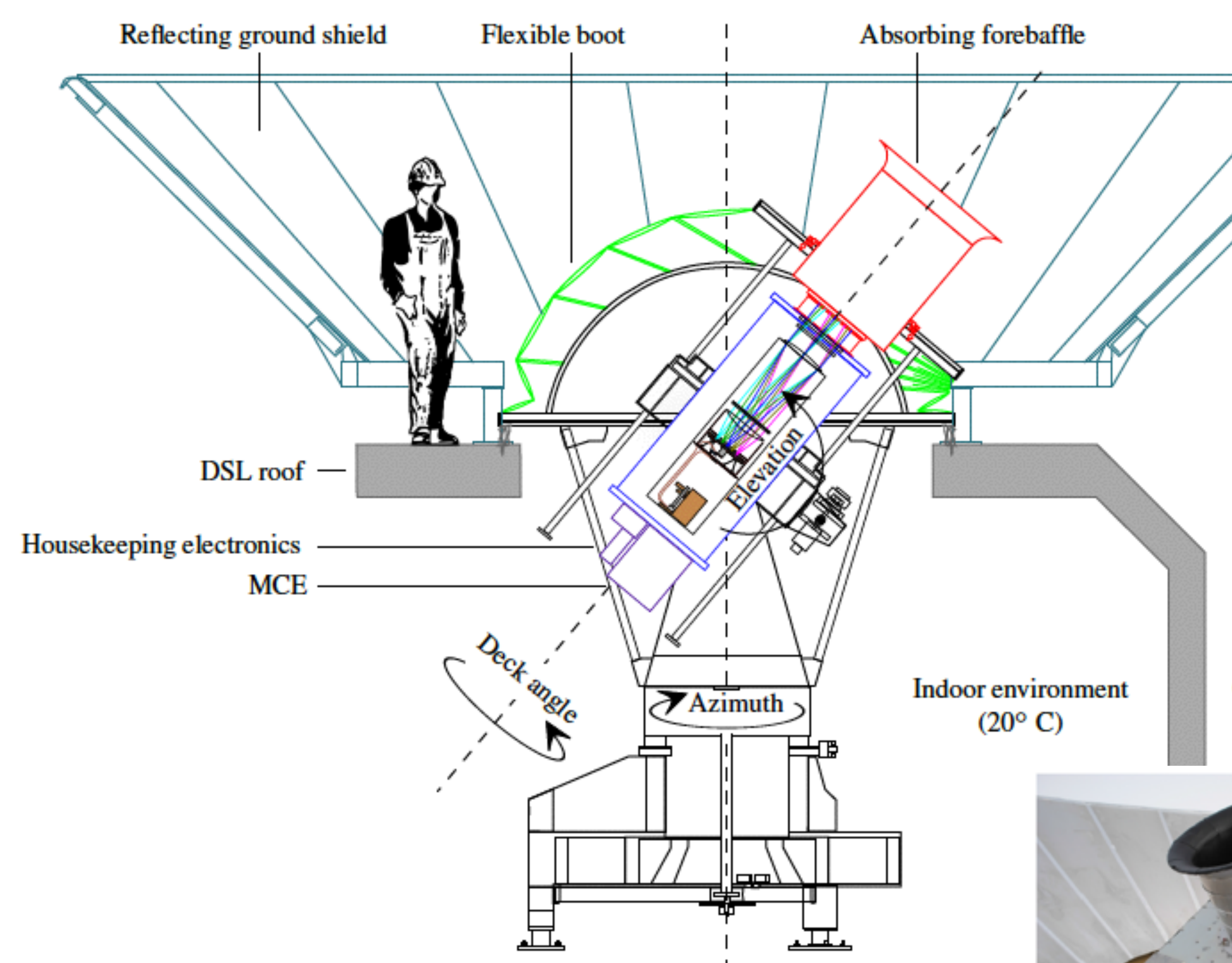

Figure 2. BICEP2 absorbing forebaffle, flexible environmental seal (the "boot"), and ground shield. The telescope and mount sat below the boot inside the Dark Sector Laboratory.

Dark Sector Laboratory (DSL) located 800 m from the South Pole

Rotation of telescope cancels many classes of systematic effect.

BICEP2

Measurement within the field in the "Southern Hole" where Galactic foreground are very low.'

Year 2010-2012

Observed only 150 GHz (λ

Polarization sensitive bolometers: 500 (from 98 in BICEP1)

Antenna-coupled transition-edge sensor (TES) arrays

Photolithographically fabricated planar device, a single monolithic silicon wafer.

Multiplexing SQUID amplifiers reduces the number of wires and the heat load.

South Pole

Housed in the Dark Sector Laboratory (DSL).

Excellent site for millimeter-wave observation from the ground

Exceptionally low water vapor, reducing atmospheric noise due to the absorption and emission of water near the 150 GHz observing band.

Very stable weather especially during the dark winter months.

Low atmospheric 1/f noise and loading

Optical System

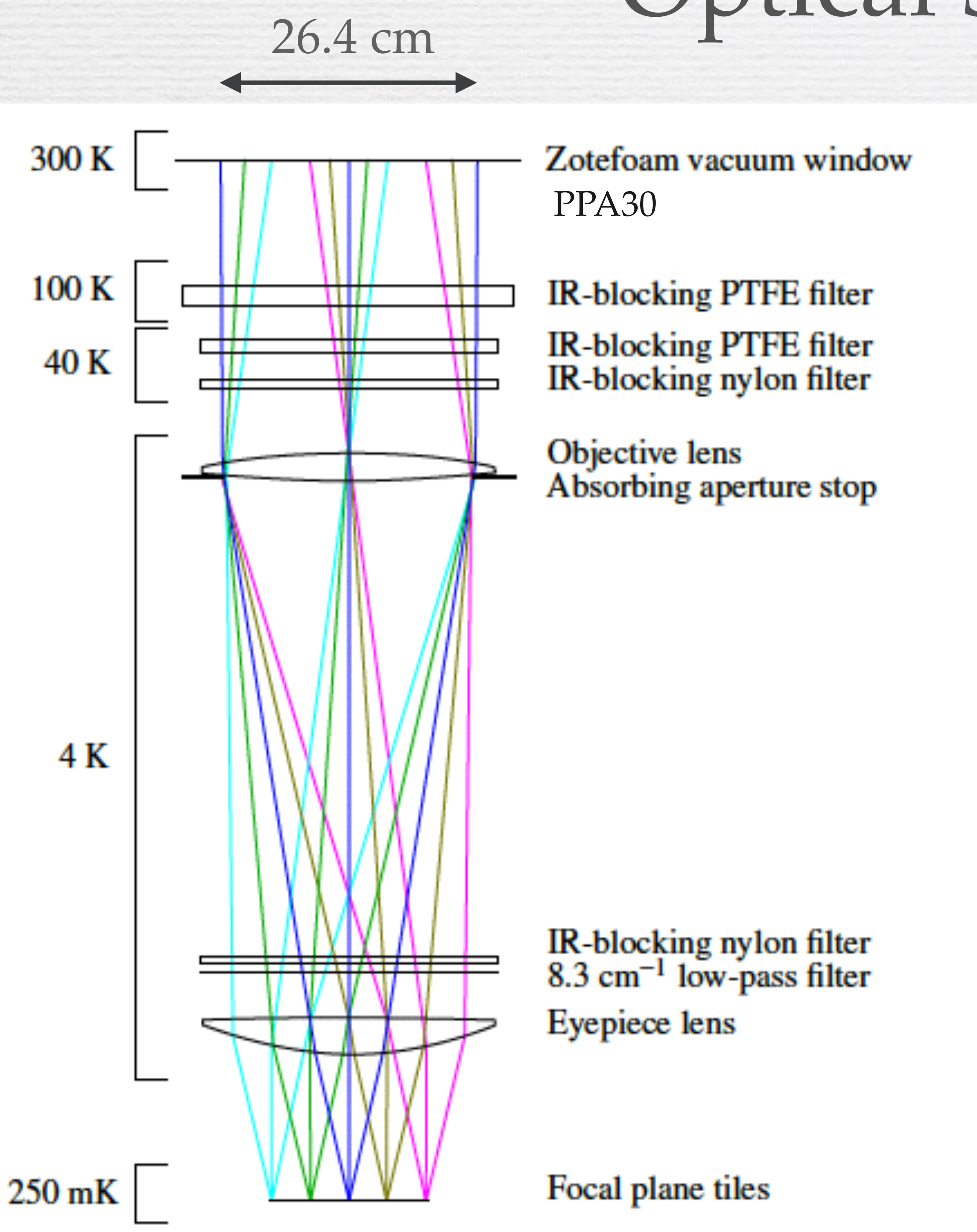

Figure 3. The telescope optical system. All components (except the window) were anti-reflection coated to provide minimal reflection at 150 GHz. All optics below the 40 K nylon filter were cooled to 4 K, providing low and stable optical loading. Due in large part to the radially symmetric design, simulations predict well-matched beams for two idealized orthogonally polarized detectors at the focal plane.

Refractive telescope avoiding reflective components that can have significant instrumental polarization.

Cooling for low optical loading.

No intrinsic cross-polar response < 0.5%

PPA30: material, closed-cell nitrogen-filled polypropylene foam with low scattering and high microwave transmission.

Polytetrafluoroethylene (PTEE) filters for absorbing the infrared radiation (IR).

Table 1
Modeled detector loading from elements in the optical path

Element	T_e [K]	Emissivity	Loading [pW]	T_{RJ} [K]
CMB	3	1.00	0.12	
Atmosphere	230	0.03	2.0	
Upper Forebaffle	230	1.00	0.65	
Window	230	0.02	1.0	
IR Blocker 1	100	0.02	0.45	
IR Blocker 2	40	0.02	0.18	
IR Blocker 3	40	0.02	0.18	
IR Blocker 4	6	0.02	0.01	
Lenses	6	0.10	0.07	
Total			4.7	22

Optical System

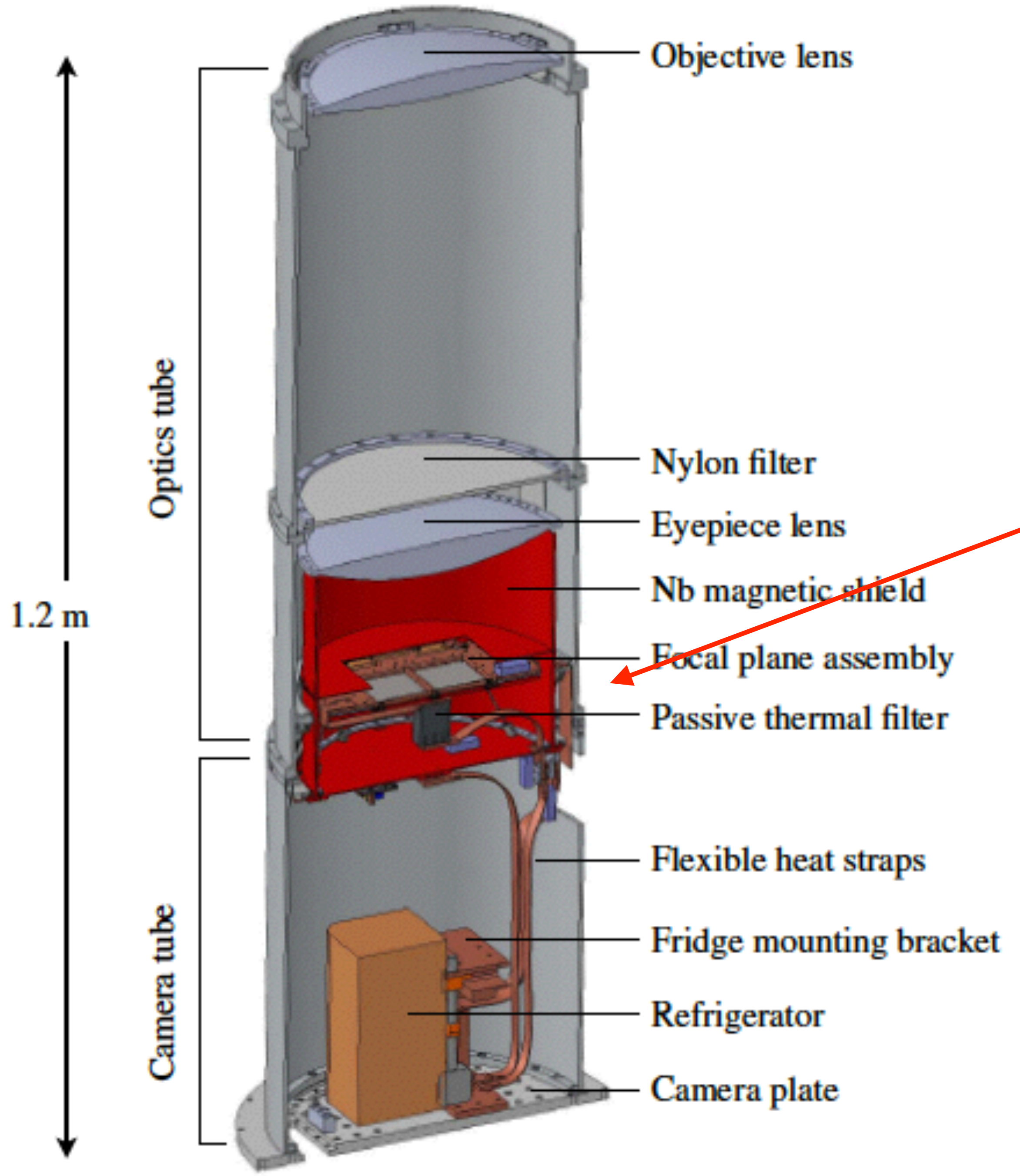

Figure 4. Cross-sectional view of the telescope insert. The entire telescope insert assembly is cooled to 4 K by a thermal link to a liquid helium bath. The optics tube provides rigid structural support for the optical chain, including the lenses, filters, and aperture stop. The camera tube assembly houses the sub-kelvin sorption refrigerator and the cryogenic readout electronics in a radiatively and thermally protected enclosure. The sub-kelvin focal plane assembly sits within a superconducting Nb magnetic shield. The focal plane is thermally connected to the fridge via a passive thermal filter.

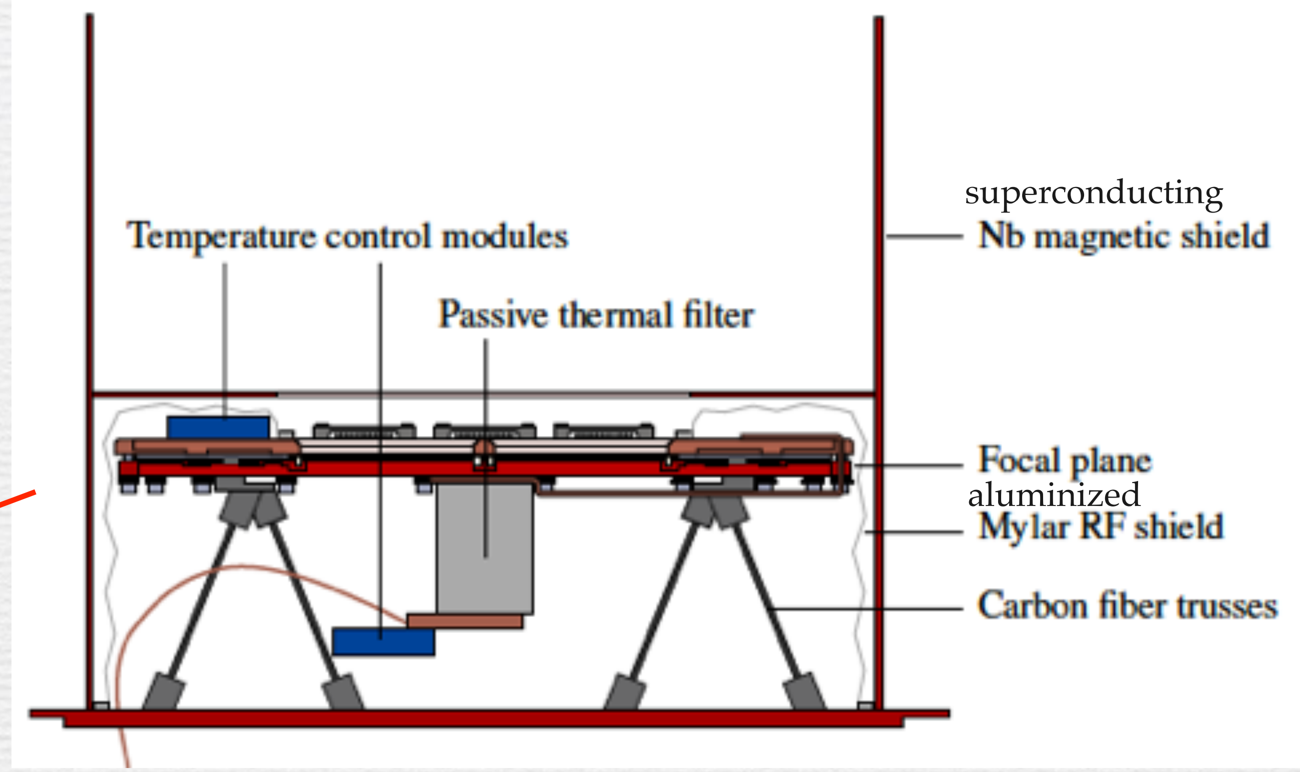

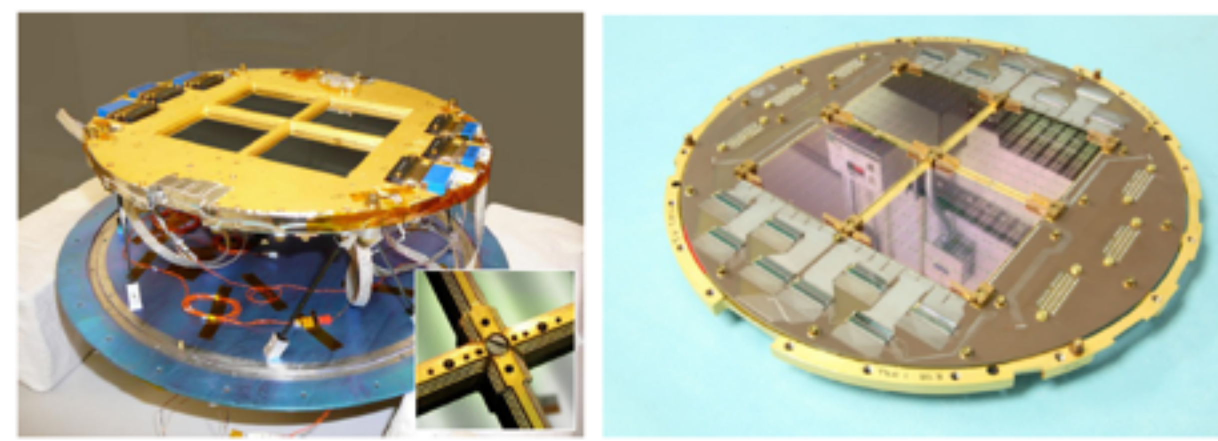

Figure 6. The assembled focal plane on the carbon fiber truss structure and 350 mK Nb plate. The four anti-reflection tiles and detector tiles sit beneath square windows in the copper plate. This assembly will be covered in the aluminized Mylar radio frequency shield, with a square opening only above the detector tiles. *Left:* Unshielded assembly; *Left inset:* Corrugations in the edges of the copper plate next to the detector tiles; *Right:* The underside of the focal plane Cu plate, with detector tiles and SQUID and Nyquist chips mounted.

Focal Plane System

band-defining filter

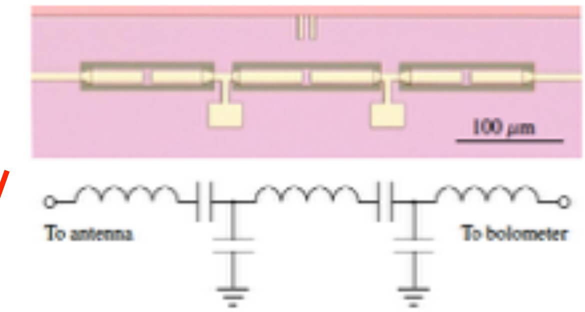

Figure 9. 150 GHz band-defining filter and equivalent circuit. Each filter consisted of three inductors in series, coupled to each other through a T-network of capacitors.

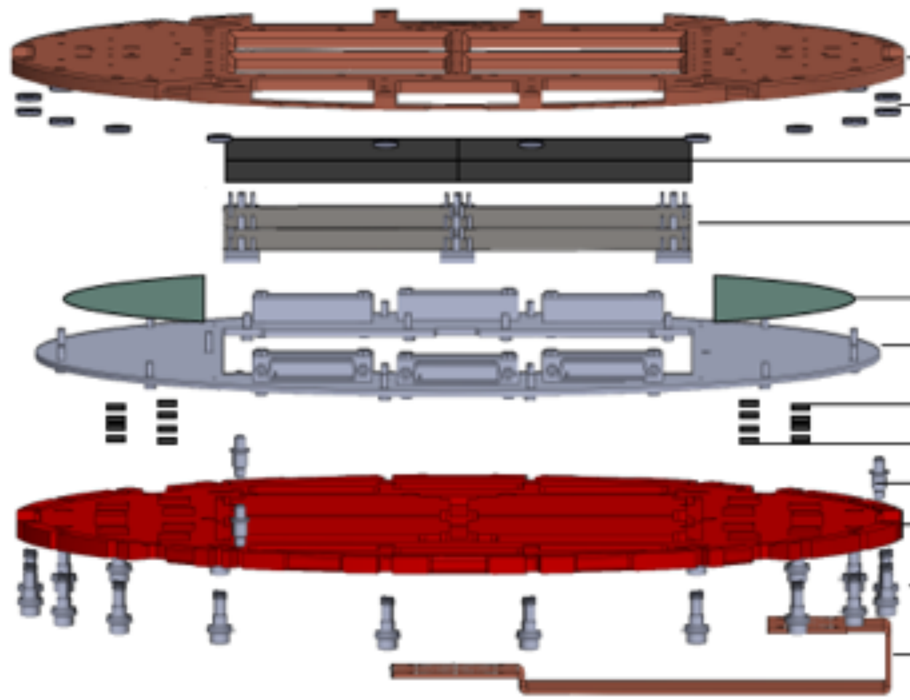

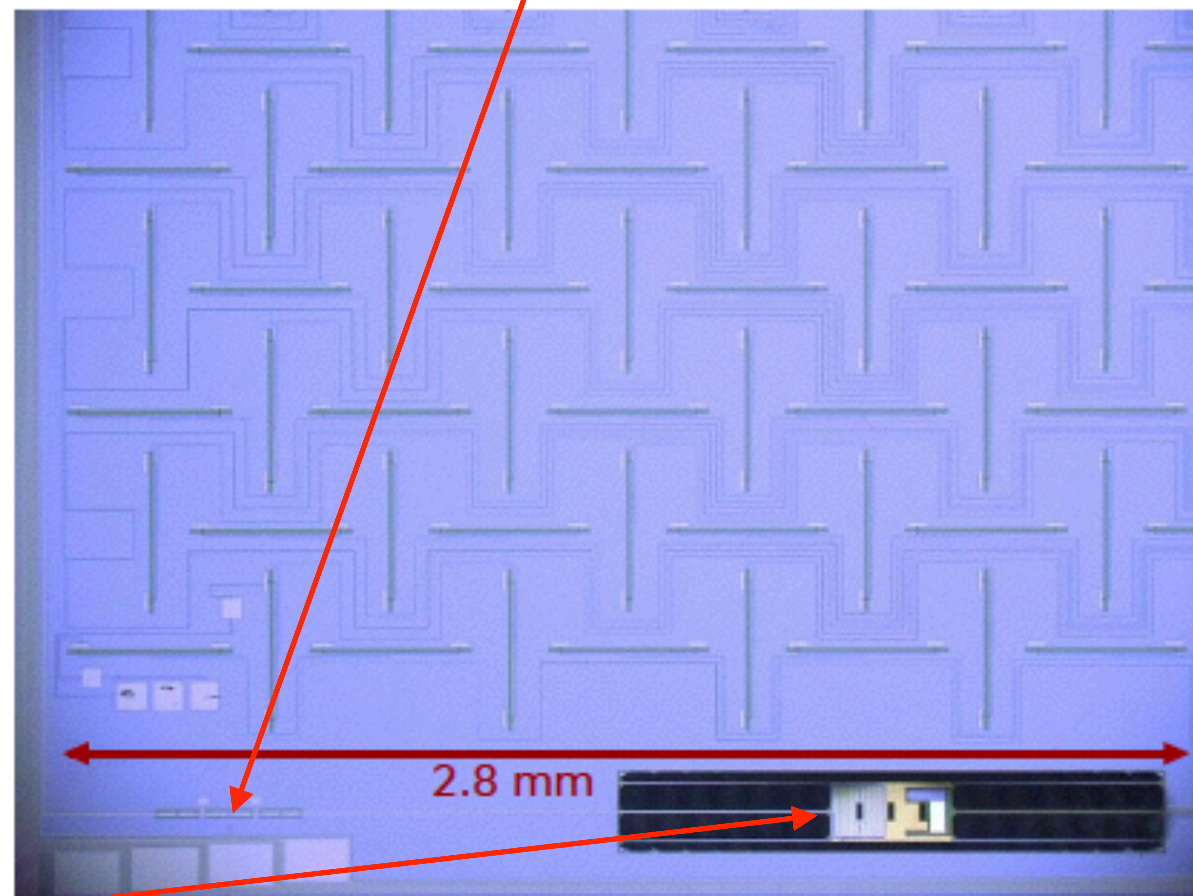

4 Tiles of 8x8 spatial pixels.
288 slots for each pixel.

Transition Edge Sensor (TES)

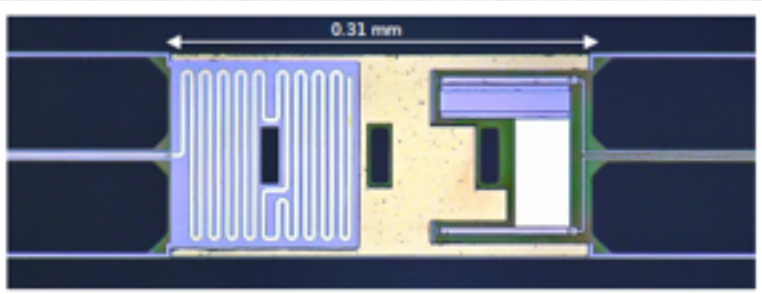

Figure 10. TES island for a single BICEP2 detector. The island was supported by six lithographically etched legs. Microwave power, entering from the left, terminated into a resistive meander. The deposited heat is measured as a decrease in electrical power (or current) dissipated in the titanium TES, which appears as a blue rectangle on the right of the island. The TES voltage bias was provided by two micro-strip lines at right. To increase the dynamic range of the device, an aluminum TES (seen as a white rectangle below the titanium film) was deposited in series with the titanium TES, providing linear response across a wide range of background loading conditions. The heat capacity of the island was tuned by adding 2.5 μm thick evaporated gold, which is distributed across the remaining real estate of the island. This made the detector time constants (§10.6) slow enough for stable operation.

Figure 8. Partial view of one BICEP2 dual-polarization pixel, showing the band-defining filter (lower left), TES island (lower right), and part of the antenna network and summing tree. The vertically oriented slots are sensitive to horizontal polarization and form the antenna network for the A detector, while the horizontally oriented slots receive vertical polarization and are fed into the B detector. In this way the A and B detectors have orthogonal polarizations but are spatially co-located and form beams that are coincident on the sky. This view corresponds to a boresight angle of 90°. At boresight angle of 0° the A detectors receive vertical polarization and the B detectors receive horizontal polarization.

Observation Schedule

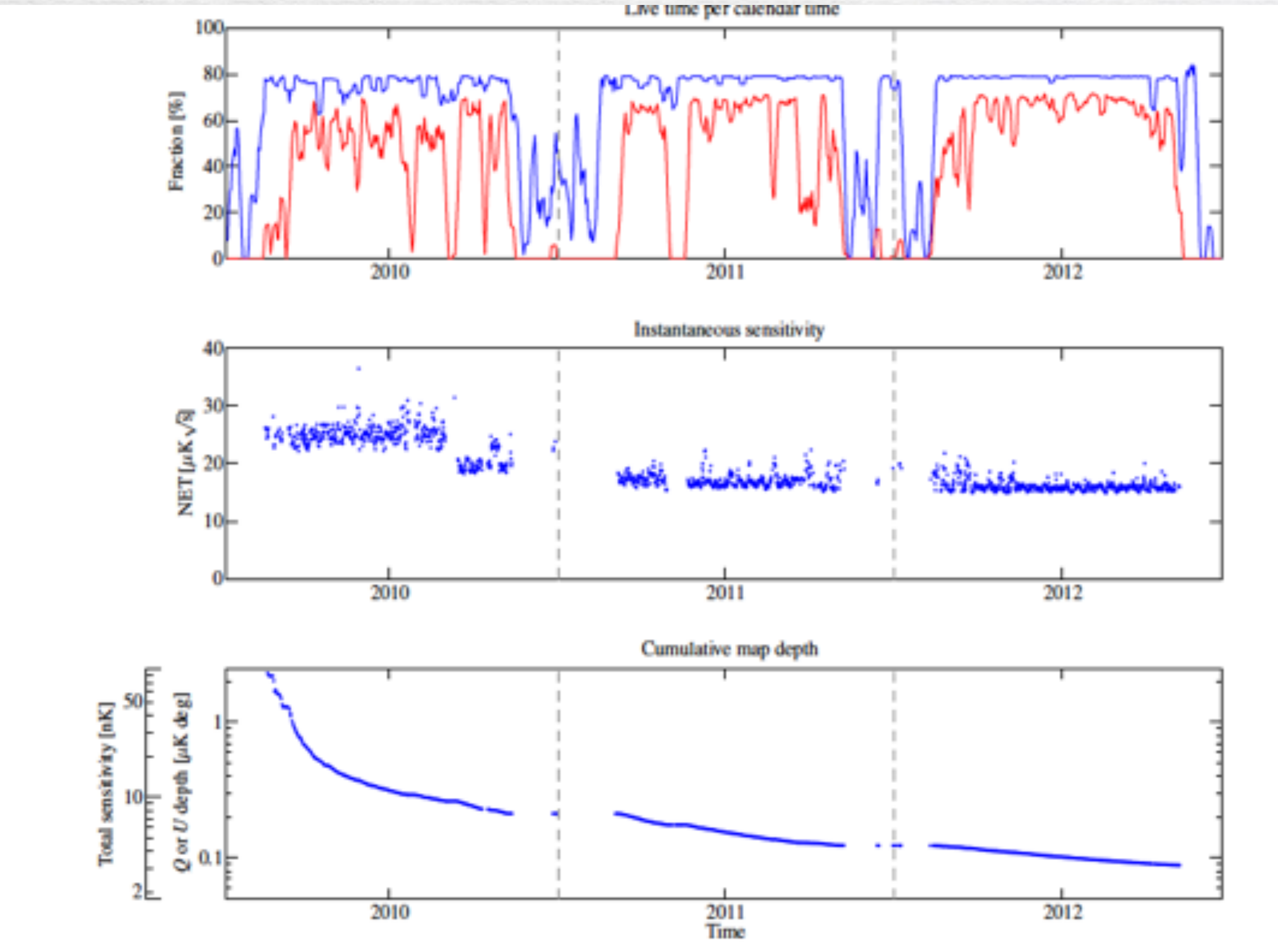

Figure 23. Integration of the BICEP2 three-year data set. *Top panel:* Time per day spent in CMB scans, regular calibrations, and refrigerator cycling. During austral summers (November–February), observing schedules have been interspersed with beam mapping and other tests and calibrations. During the austral winter, on-source efficiency (including Galactic observations) has been high, never falling far below the ideal 79.2% in the winter of 2012. The lower, red curve includes data quality cuts. *Middle panel:* Mapping speed over time. The improvement from early to late 2010 was caused by the optimization of TES biases (§10.5), the improvement from 2010 to 2011 was caused by the change to 25 kHz multiplexing (§9.3), and the small improvement from 2011 to 2012 was caused by a small increase in the number of active channels (§11.6). Each data point represents one observing phase of six or nine hours, as described in Section 12.3. *Bottom panel:* Cumulative map depth over time as calculated in §14.2.

Low foreground region
centered at RA 0h, Dec. -57.5 deg

Right Ascension -50 to 50 deg
Declination. -55 to -60 deg

In total ~590 days of observation in three years.

~50 minute "scan set", which has
53 times back and forth azimuthal movement.

→

~3 days for one full scanning.

Table 8
Sensitivity by season

Season	Time [10^6 s]	Integration [10^9 det·s]	Map depth [nK·deg]	Total sensitivity [nK]
2010	8.1	2.3	213.2	7.70
2011	8.5	2.6	148.6	5.37
2012	11.0	3.7	124.0	4.47
Total	27.6	8.6	87.8	3.15

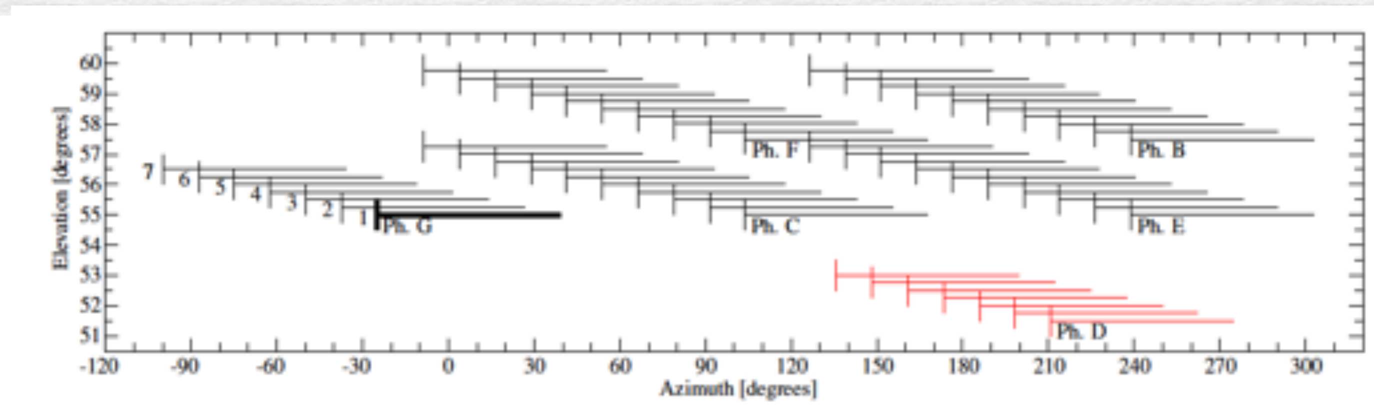

Figure 21. Observing pattern of a typical three-day schedule. Phase letters are as in Table 6. The scansets of Phase G are numbered, with the first scanset at the lowest elevation. The first scanset of Phase G is shown in bold, showing the throw of the field scans (horizontal line) and the bracketing elevation nods (vertical line). The two six-hour phases can vary in elevation: the Galactic D phase is shown at the lowest of four elevation steps, and the CMB G phase is shown at the lowest of three elevation steps. The H and I phases on the third LST day alternate between the B/C pattern and the E/F pattern.

Calibration

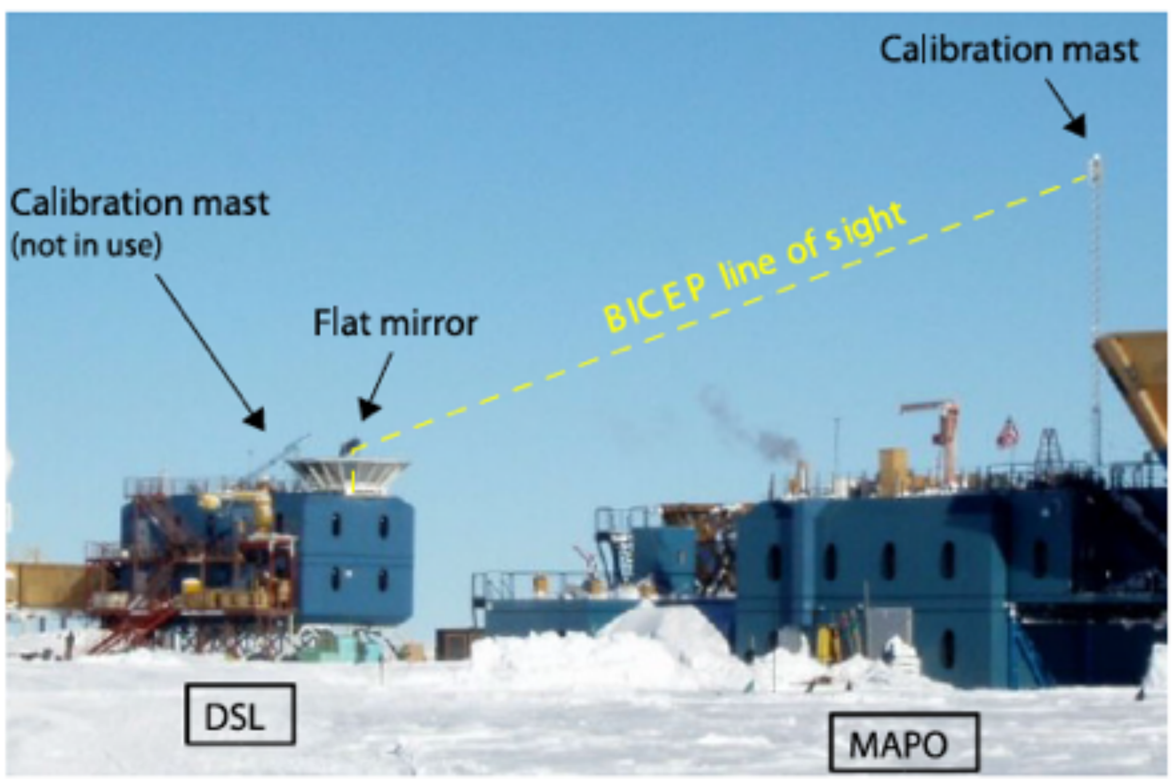

Figure 8. Beam mapping setup on site consisted of sources mounted on the top of fold-over masts. When using the mast on the MAPO building (200 m from the DSL), a flat mirror is mounted to direct the beams over the ground screen.

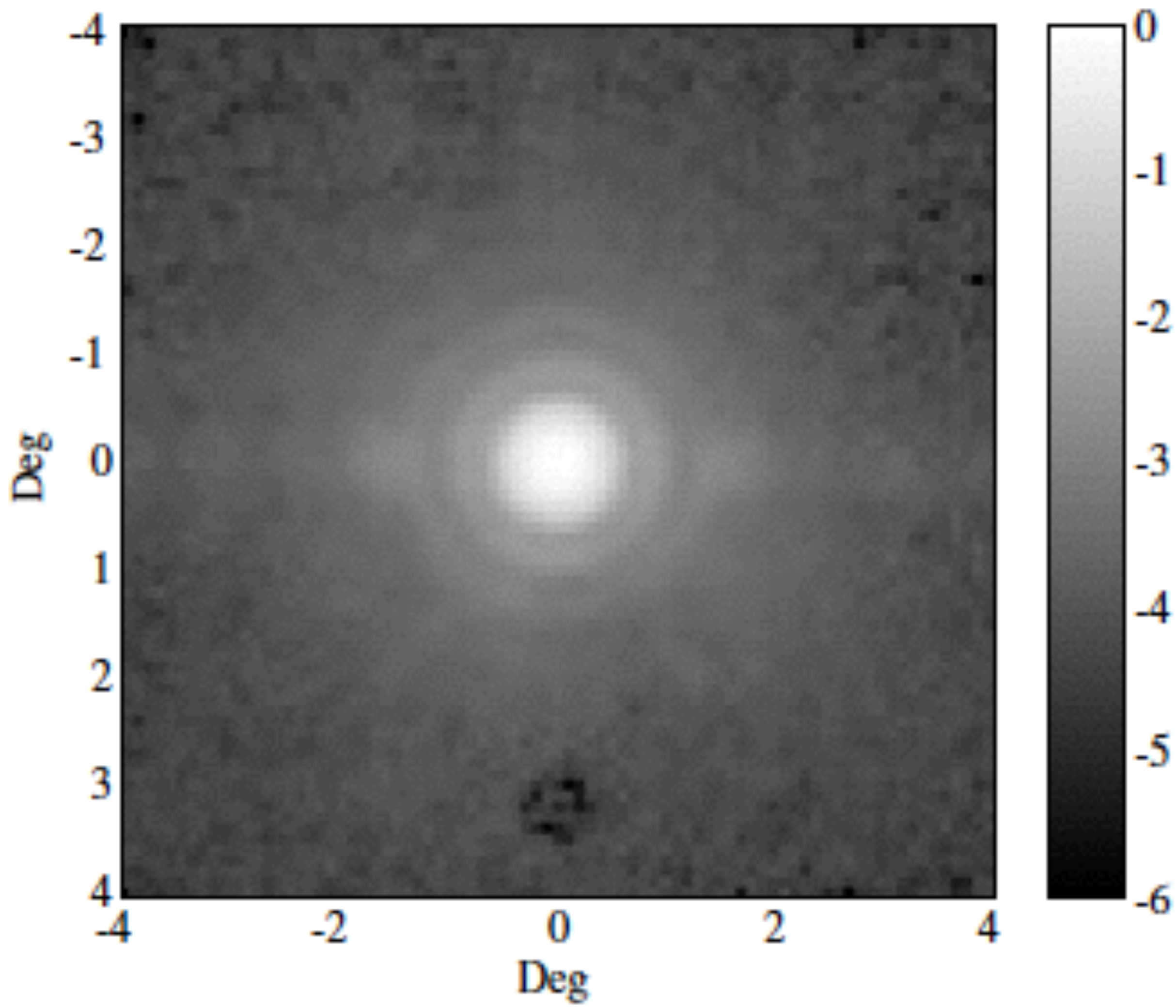

Figure 17. A map of the BICEP2 far-field response made with the thermal source in units of $\log_{10}$(power), showing dynamic range of more than six decades. Beam maps for individual detectors are shifted to align the peaks and coadded over all operational detectors. The measured shape of the main beam and Airy ring structure are well matched by simulations, as shown in the Beams Paper. Crosstalk features are apparent as small additional beams to the left and right, at a low level relative to the main beam strength. The dark feature near the bottom is negative-going crosstalk found only in a subset of channels.

Result E/B-Mode Map

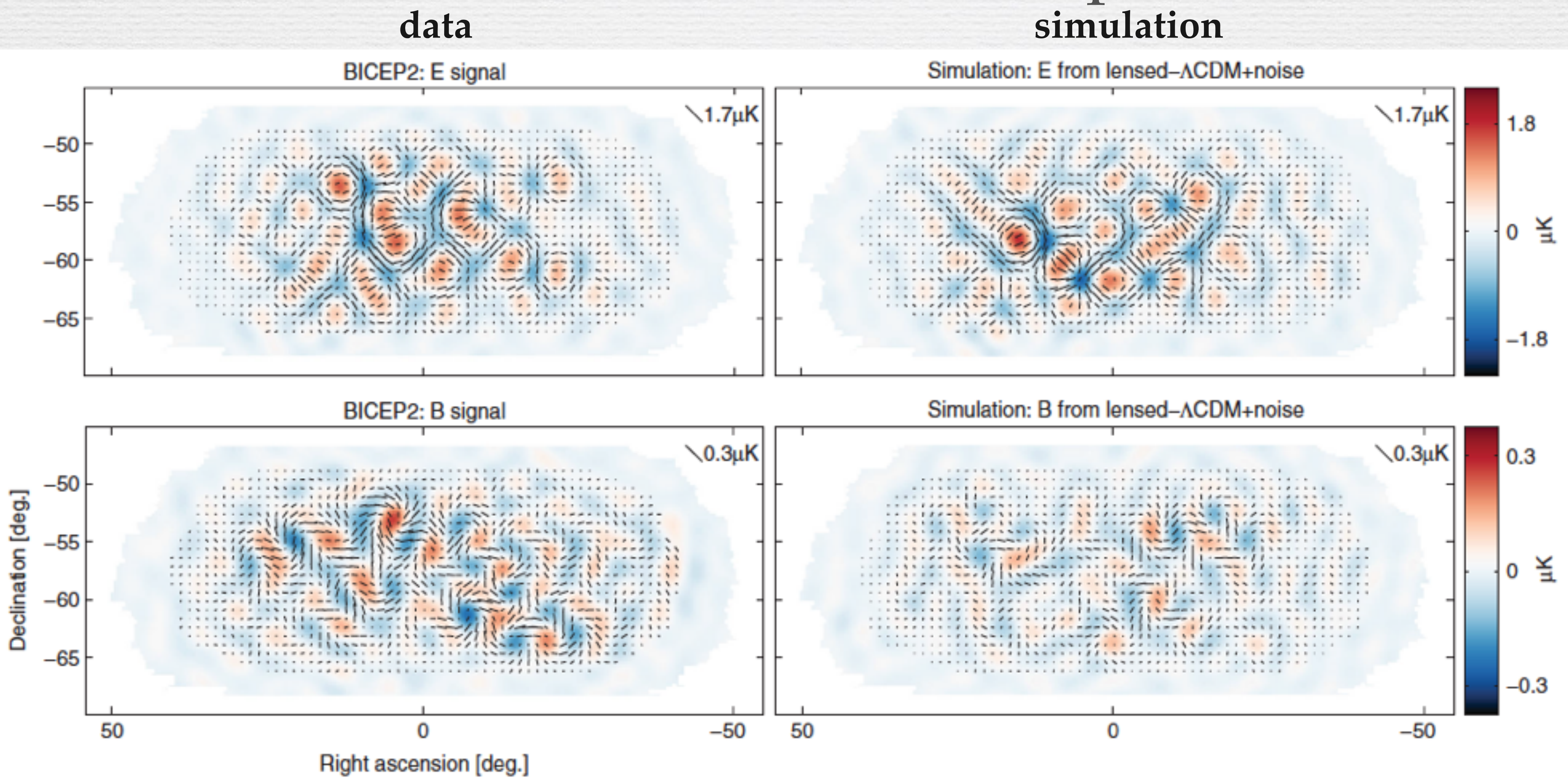

FIG. 3 (color). Left: BICEP2 apodized E-mode and B-mode maps filtered to $50 < \ell < 120$. Right: The equivalent maps for the first of the lensed-ΛCDM + noise simulations. The color scale displays the E-mode scalar and B-mode pseudoscalar patterns while the lines display the equivalent magnitude and orientation of linear polarization. Note that excess B mode is detected over lensing+noise with high signal-to-noise ratio in the map ($s/n > 2$ per map mode at $\ell \approx 70$). (Also note that the E-mode and B-mode maps use different color and length scales.)

Result E/B-Mode Map

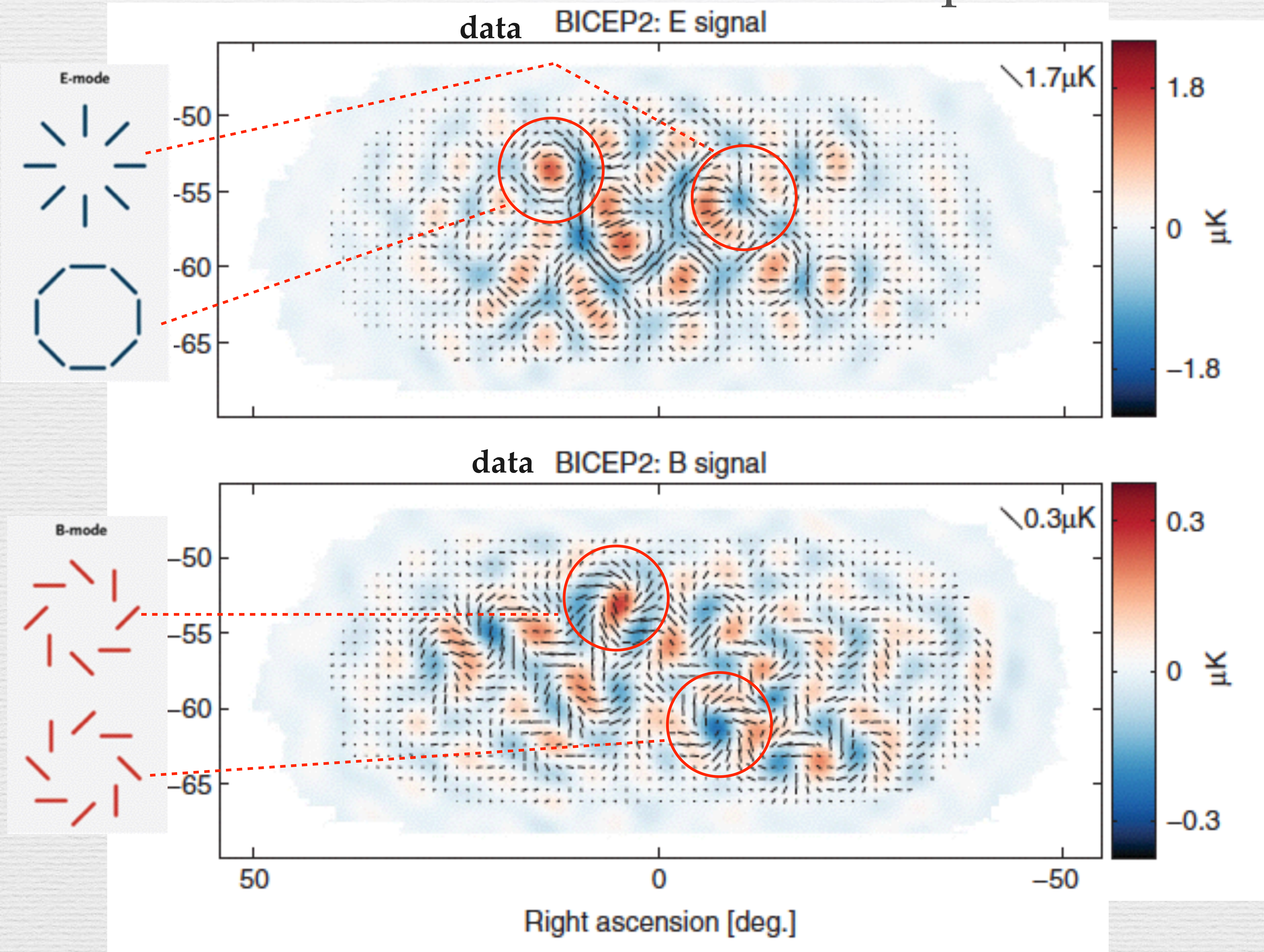

Result T/E/B Multipole Correlations

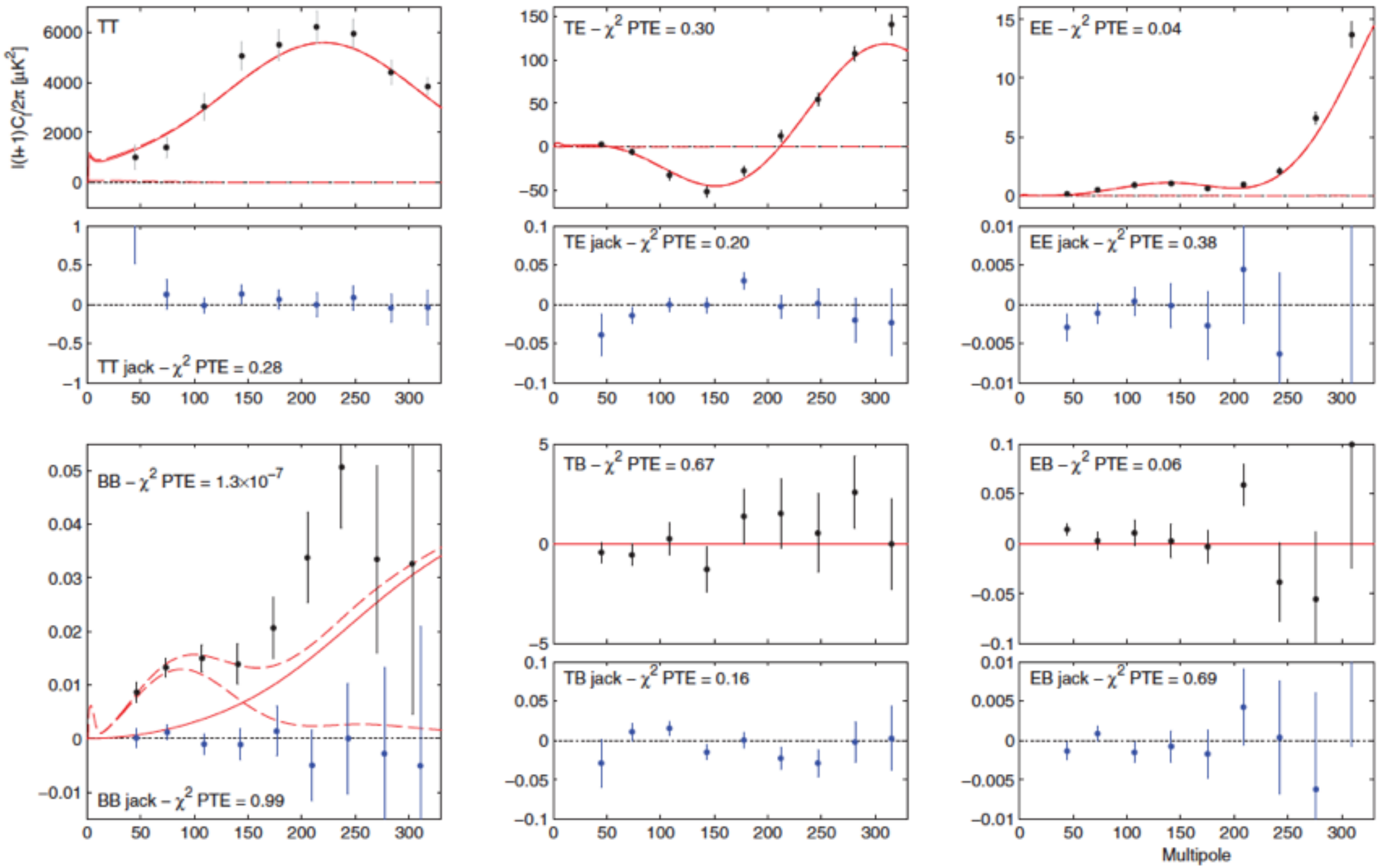

FIG. 2 (color). BICEP2 power spectrum results for signal (black points) and temporal-split jackknife (blue points). The solid red curves show the lensed-ΛCDM theory expectations while the dashed red curves show $r = 0.2$ tensor spectra and the sum of both. The error bars are the standard deviations of the lensed-ΛCDM + noise simulations and hence contain no sample variance on tensors. The probability to exceed (PTE) the observed value of a simple χ^2 statistic is given (as evaluated against the simulations). Note the very different y-axis scales for the jackknife spectra (other than BB). See the text for additional discussion of the BB spectrum. (Note that the calibration procedure uses EB to set the overall polarization angle so TB and EB as plotted above cannot be used to measure astrophysical polarization rotation—see Sec. VIII B.)

BICEPT2 BB Autocorrelation Spectrum

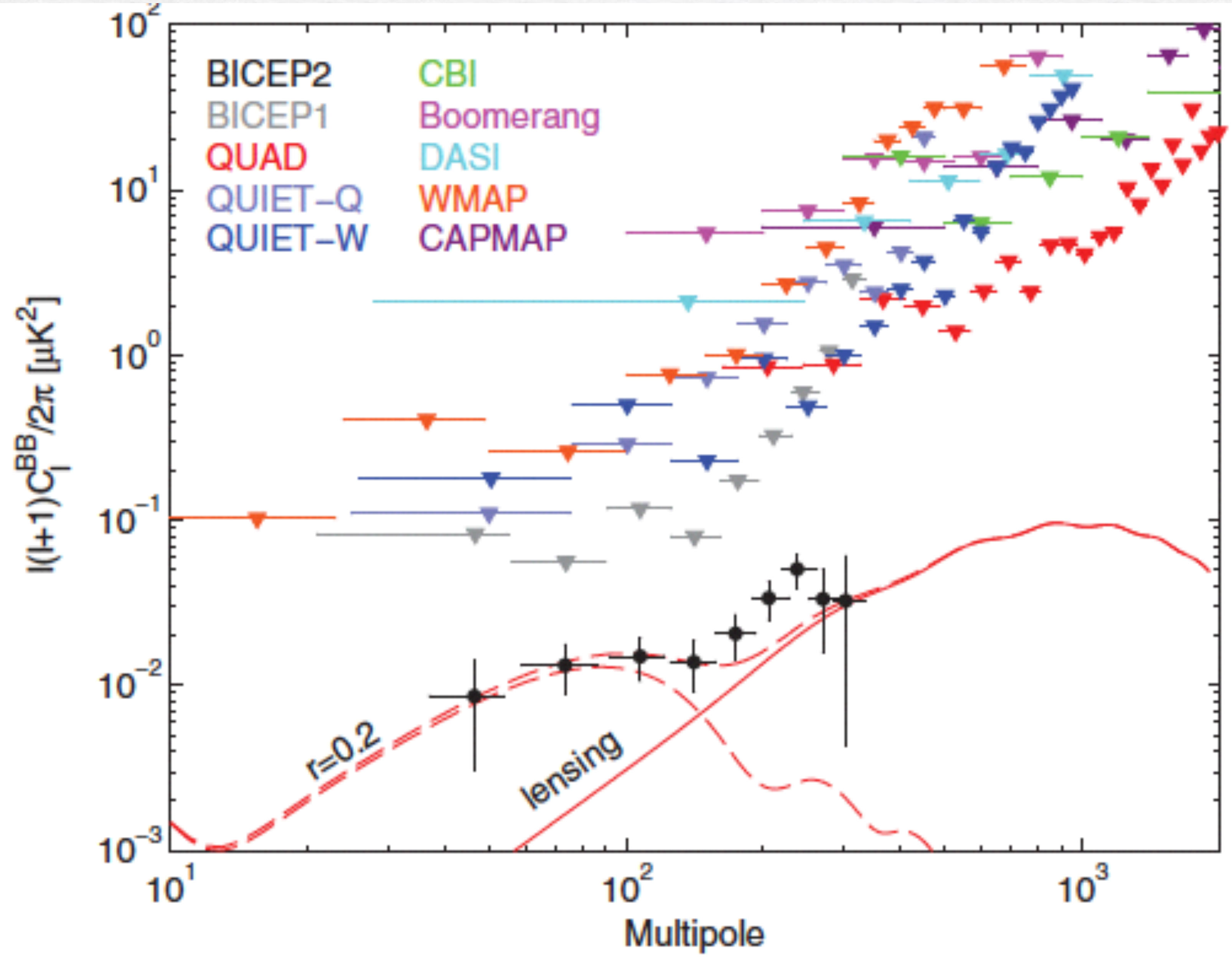

FIG. 14 (color). BICEP2 *BB* auto spectra and 95% upper limits from several previous experiments [2,40,42,43,47,49–51,107]. The curves show the theory expectations for $r = 0.2$ and lensed ΛCDM. The BICEP2 uncertainties include sample variance on an $r = 0.2$ contribution.

Foregrounds

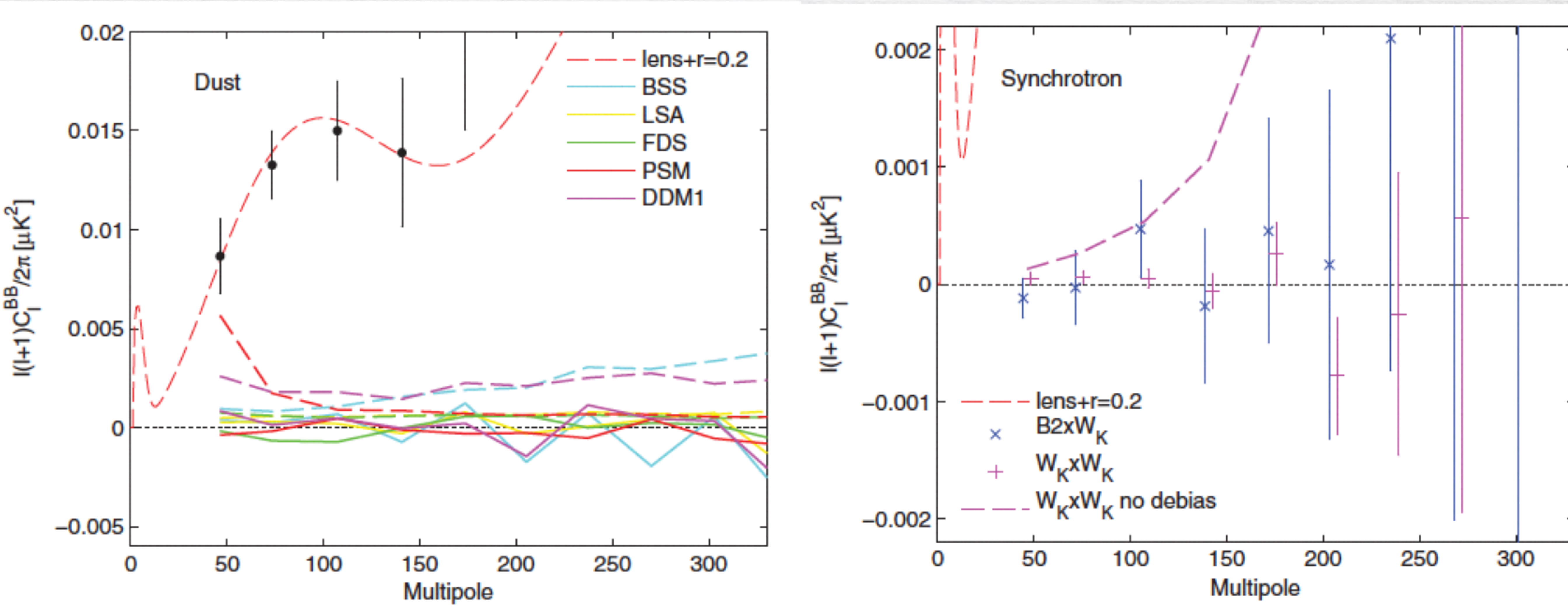

FIG. 6 (color). Upper: Polarized dust foreground projections for our field using various models available in the literature, and a new one formulated using the information officially available from *Planck*. Dashed lines show autospectra of the models, while solid lines show cross spectra between the models and the BICEP2 maps. The BICEP2 auto spectrum from Fig. 2 is also shown with the lensed-ΛCDM $+ r = 0.2$ spectrum. Lower: Polarized synchrotron constraints for our field using the WMAP K band (23 GHz) maps projected to 150 GHz using the mean spectral index within our field ($\beta = -3.3$) from WMAP. The blue points with error bars show the cross spectrum between the BICEP2 and WMAP maps, with the uncertainty estimated from cross spectra against simulations of the WMAP noise. The magenta points with error bars and the dashed curve show the WMAP auto spectrum with and without noise debias. See the text for further details.

Note added:

Since we submitted this paper new information on polarized dust emission has become available from the Planck experiment in a series of papers

Thus while these papers do not offer definitive information on the level of dust contamination in our field, they do suggest that it may well be higher than any of the models considered in Sec.

More data are clearly required to resolve the situation.
We note that cross-correlation of our maps with the Planck 353 GHz maps will be more powerful than use of those

Planck, new release on the polarized dust

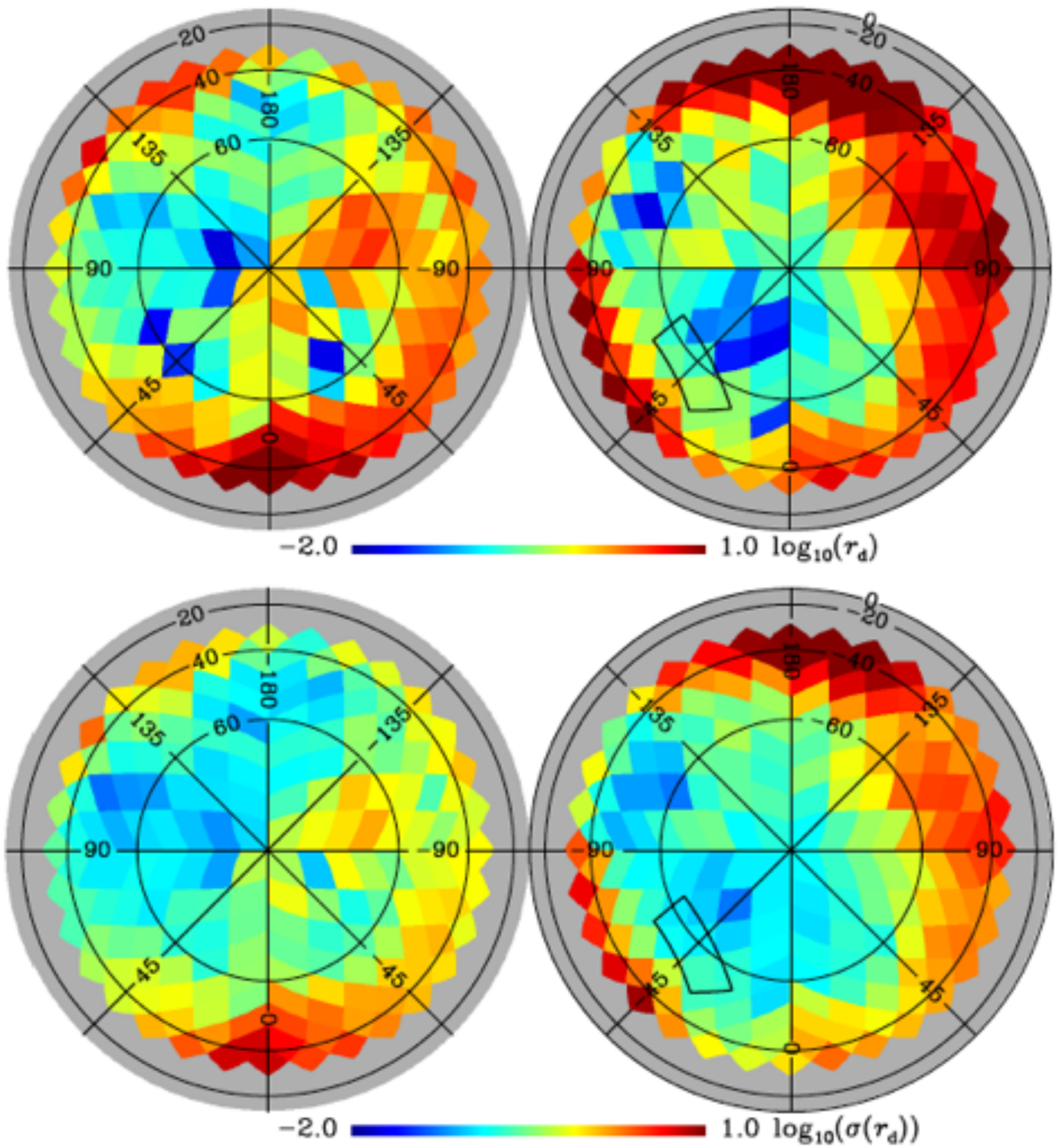

Fig. 8: *Top*: map in orthographic projection of the 150 GHz $\mathcal{D}_\ell^{BB}$ amplitudes at $\ell = 80$, computed from the *Planck* 353 GHz data, extrapolated to 150 GHz, and normalized by the CMB expectation for tensor-to-scalar ratio $r = 1$. The colours represent the estimated contamination from dust in r_d units (see details in Sect. 5.3). The logarithm of the absolute value of r_d for a 400 deg^2 patch is presented in the pixel on which the patch is centred. As described in Sect. 3.3.2, the patches overlap and so their properties are not independent. The northern (southern) Galactic hemisphere is on the left (right). The thick black contour outlines the approximate BICEP2 deep-field region (see Sect. 6). *Bottom*: associated uncertainty, $\sigma(r_d)$.

R. Adam et al., arXiv:1409.5738v1 (2014)

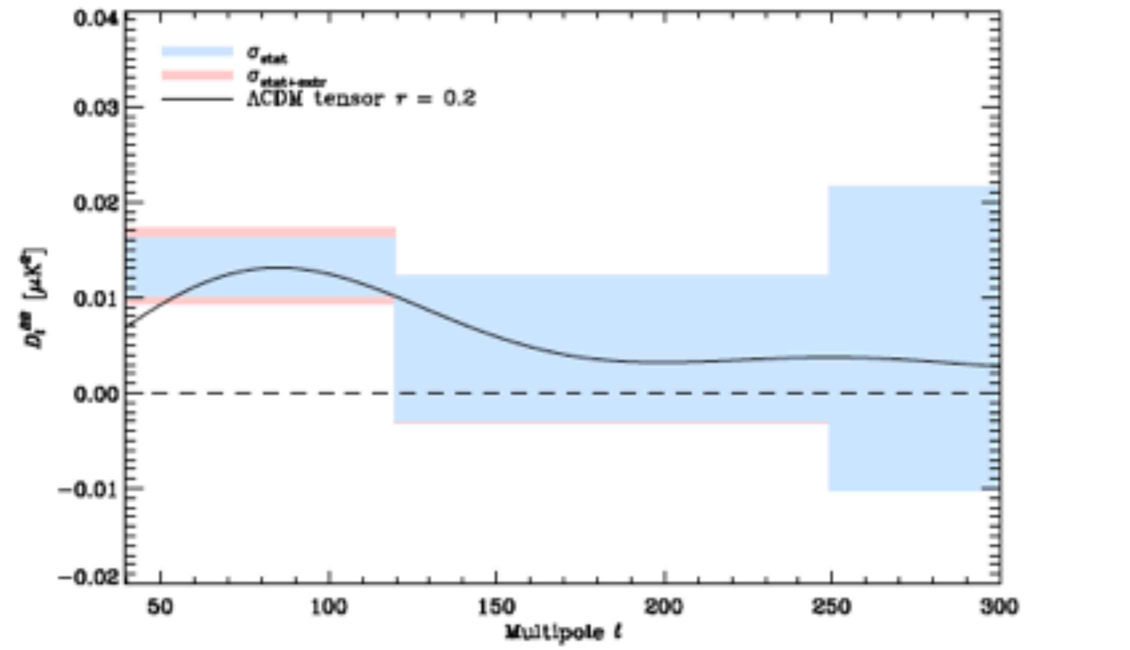

Fig. 9: *Planck* 353 GHz $\mathcal{D}_\ell^{BB}$ angular power spectrum computed on M_{B2} defined in Sect. 6.1 and extrapolated to 150 GHz (box centres). The shaded boxes represent the $\pm 1\sigma$ uncertainties: blue for the statistical uncertainties from noise; and red adding in quadrature the uncertainty from the extrapolation to 150 GHz. The *Planck* 2013 best-fit ΛCDM $\mathcal{D}_\ell^{BB}$ CMB model based on temperature anisotropies, with a tensor amplitude fixed at $r = 0.2$, is overplotted as a black line.

Yet, it is not converged.

Nature of Reality 21 Oct 2014
Last month, new data released by the Planck team confirmed that all or most of the BICEP2 signal could indeed be due to dust. It doesn't rule out the possibility that BICEP2 saw something real, but shows that the signal can't yet be untangled from the noise.

Editors of Nature reacted in an October 14 editorial:

As we have pointed out before, researchers must not be afraid to be wrong. With hindsight they may feel they rushed to publish their claim too quickly, but professional science is a competitive and fast-moving field. The academic paper was cautious and the team's reaction to subsequent criticism seems constructive.

POLARBEAR
Berkeley physicist Adrian Lee, explains the first successful isolation of a "B-mode" produced by **gravitational lensing**

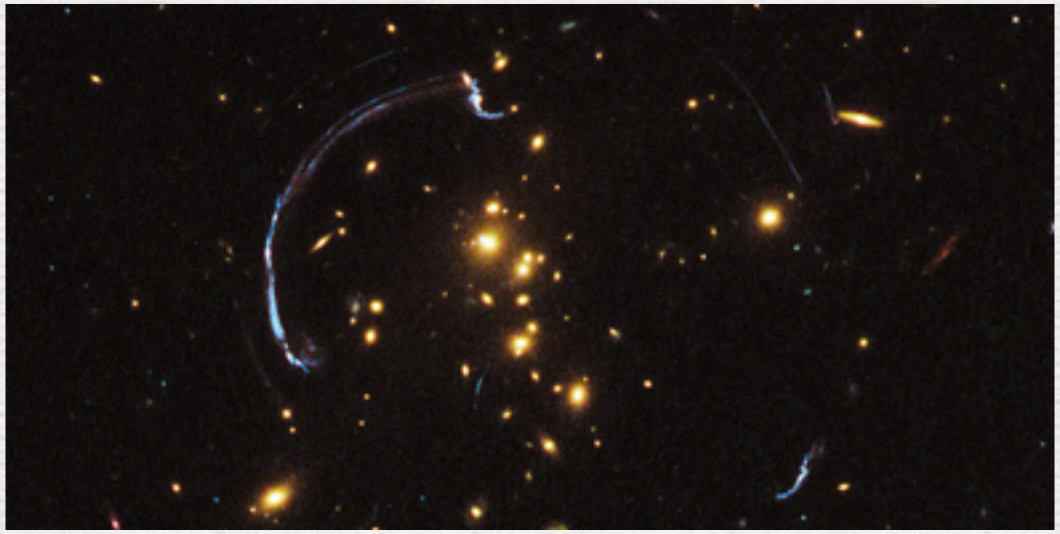

References

1. 長島順清「高エネルギー物理学の発展」朝倉書店
2. Newton
3. 佐藤勝彦「インフレーション宇宙論」ブルーバックス、講談社
4. A CMB Polarization Primer by W. Hu and M. White, Princeton 1997 http://background.uchicago.edu/~whu/polar/webversion/polar.html

See also